remote sensing

MDPI

Article

Seasonal and Diurnal Characteristics of the Vertical Profile of Aerosol Optical Properties in Urban Beijing, 2017–2021

Xinglu Zhang [1], Yu Zheng [1,2], Huizheng Che [1,*], Ke Gui [1], Lei Li [1], Hujia Zhao [3], Yuanxin Liang [1,4], Wenrui Yao [1,4], Xindan Zhang [1,4], Hengheng Zhao [1], Yanting Lu [1,5] and Xiaoye Zhang [1]

[1] State Key Laboratory of Severe Weather & Key Laboratory of Atmospheric Chemistry, Institute of Atmospheric Composition and Environmental Meteorology, Chinese Academy of Meteorological Sciences, China Meteorological Administration, Beijing 100081, China
[2] Collaborative Innovation Center on Forecast and Evaluation of Meteorological Disasters (CIC-FEMD), Nanjing University of Information Science & Technology, Nanjing 210044, China
[3] Institute of Atmospheric Environment, China Meteorological Administration, Shenyang 110166, China
[4] Department of Atmospheric and Oceanic Sciences & Institute of Atmospheric Sciences, Fudan University, Shanghai 200438, China
[5] Meteorological Impact and Risk Research Center, Chinese Academy of Meteorological Sciences, Beijing 100081, China
* Correspondence: chehz@cma.gov.cn

Abstract: Seasonal and diurnal characteristics of the vertical profiles of aerosol properties are essential for detecting the regional transport and the climatic radiative effects of aerosol particles. We have studied the seasonal and diurnal characteristics of the vertical distribution of aerosols in urban Beijing from 2017 to 2021 based on long-term Raman–Mie LiDAR observations. The influence of the vertical distribution of aerosols, the meteorological conditions within the boundary layer, the optical–radiometric properties of aerosols, and their interconnections, were investigated during a heavy haze pollution event in Beijing from 8 to 15 February 2020 using both meteorological and sun photometer data. The aerosol extinction coefficient was highest in summer (0.4 km^{-1}), followed by winter (0.35 km^{-1}), and roughly equal in spring and autumn (0.3 km^{-1}). The aerosol extinction coefficient showed clear daily variations and was different in different seasons as a result of the variation in the height of the boundary layer. During the haze pollution event, the particulate matter mainly consisted of scattered spherical fine particles and the accumulation time of pollutants measured via the AOD_{440nm} and $PM_{2.5}$ mass concentration was different as a result of the hygroscopic growth of the aerosol particles. This growth increased scattering and led to an increase in the aerosol optical depth. The vertical transport of particulate matter also contributed to the increase in the aerosol optical depth.

Keywords: aerosol vertical distribution; aerosol optical properties; haze; Beijing

check for updates

Citation: Zhang, X.; Zheng, Y.; Che, H.; Gui, K.; Li, L.; Zhao, H.; Liang, Y.; Yao, W.; Zhang, X.; Zhao, H.; et al. Seasonal and Diurnal Characteristics of the Vertical Profile of Aerosol Optical Properties in Urban Beijing, 2017–2021. *Remote Sens.* **2023**, *15*, 475. https://doi.org/10.3390/rs15020475

Academic Editor: Cheng Liu

Received: 8 December 2022
Revised: 31 December 2022
Accepted: 2 January 2023
Published: 13 January 2023

Copyright: © 2023 by the authors. Licensee MDPI, Basel, Switzerland. This article is an open access article distributed under the terms and conditions of the Creative Commons Attribution (CC BY) license (https://creativecommons.org/licenses/by/4.0/).

1. Introduction

"Aerosol" is a general term used to describe suspended solid and liquid particles in the atmosphere. The multi-phase system consisting of aerosols and the atmosphere, with diameters ranging from 0.001 to 100 μm, is referred to as atmospheric aerosols [1,2]. Aerosols form haze pollution, which affects both visibility and human health, after accumulating to a certain concentration under certain meteorological conditions [3–9]. Aerosols can affect the radiation balance of the Earth–atmosphere system through direct effects and can also indirectly affect the regional and global climate by influencing the microphysical properties and life cycles of clouds [10–16]. Aerosols have a crucial role in climate change at both regional and global scales, but there is considerable uncertainty in the assessment of the strength and importance of their effects [17–20]. The study of the optical–radiative properties of aerosols is one of the key solutions to reducing the uncertainties in aerosol radiative forcing.

The radiative power and effects of aerosols depend on their physical and optical properties and therefore studying these properties provides important information for predicting regional and global climate change [21]. Global long-term, ground-based observation networks (e.g., AERONET) and China's CARSNET (China Aerosol Remote Sensing Network) have provided an observational basis for understanding changes in the spatial distribution of aerosols and have improved our understanding of the impact of aerosols on regional and global climate change [11,14,22]. However, there have been few studies of the vertical distribution of aerosols [23]. The vertical distribution of aerosols can change the vertical variation of the aerosol radiative heating rate and affect atmospheric stability, which, in turn, affects the generation and development of turbulence and clouds [24–27]. The vertical distribution of aerosols can also indicate the level of pollution and the evolution of pollution processes in a defined area [28,29]. Studies of the vertical distribution of aerosols are therefore important in improving boundary layer schemes, analyses of the mechanism of pollution processes, determining the boundary layer height and in predicting air quality [30,31].

The rapid development of China's economy in recent years has led to much research on the causes of aerosol pollution and the optical properties of aerosols, especially in urban areas where high aerosol loads lead to reduced visibility, reduced solar radiation and frequent pollution events [32–38]. The meteorological conditions have a crucial role in ambient air pollution by both directly and indirectly influencing the emission, transport, formation and deposition of air pollutants [39–41]. Previous studies have found that the response of air quality to single or multiple meteorological factors varies by both city and season, with significant north–south differences in the response to humidity and wind speed [41–45]. Detailed information about the meteorological conditions within the boundary layer is therefore needed to investigate the influence of meteorological conditions within this layer on pollution events. This will help our understanding of the causes of pollution and the development of pollution prevention policies [46].

The Beijing–Tianjin–Hebei region is an important economic zone in northern China. Extreme haze events have frequently broken out in this region in recent years, causing great public concern [47–49]. Heavy pollution events (HPEs) were studied in the Beijing area during autumn and winter in 2017–2020 and the HPEs were divided into an early transport stage and a cumulating stage [49–55]. Southerly winds prevailed in the Beijing area during the transport stage and pollutants from south of Beijing were transported to the city. The solar radiation reaching the near-ground layer was reduced in the cumulating phase as a result of the extinction effect of particulate matter. This generated or enhanced the inversion layer and increased the relative humidity, which, in turn, inhibited turbulence, decreased the height of the boundary layer and inhibited the diffusion of pollutants. The higher relative humidity also promoted the hygroscopic growth of aerosols, accelerated liquid-phase and non-homogeneous-phase reactions, and increased the concentration of pollutants. This, in turn, led to a further deterioration in the meteorological conditions within the boundary layer. This two-way feedback mechanism has an important role in the formation and maintenance of heavy pollution in Beijing.

Most of the rapid increase in pollutants in these studies started from around 12:00 to 17:00 [49–55]. However, most studies have been based on overall measurements of a vertical atmospheric column without considering the vertical distribution of aerosols. There have been relatively few studies on the optical properties of aerosols and their influence on the development of pollution on a vertical scale. We therefore need detailed information on the vertical distribution and optical properties of aerosols to further investigate their interconnection with, and influence on, the meteorological conditions in the boundary layer. This will help us to improve and validate numerical models and satellite data [23].

We obtained vertical profiles of the aerosol extinction coefficient from long-term observations at the Raman–Mie LiDAR system located at the Chinese Academy of Meteorological Sciences (CAMS) from September 2017 to February 2021. We used these profiles to represent the vertical distribution of aerosols and studied the temporal variation of the vertical

distribution of aerosols in urban Beijing. We then explored the interconnections between the vertical distribution of aerosols, their optical properties and the meteorological conditions within the boundary layer during HPEs in Beijing from 8 to 15 February 2020. These results not only enrich our understanding of the regional climate and the influence of local pollution events, but also contribute to validating numerical simulation results and improving LiDAR algorithms.

The remainder of this paper is organized as follows. Section 2 describes the observational sites, data and methods. Section 3 presents the climatological characteristics of the vertical distribution of aerosols and the interconnections between the vertical distribution of aerosols, their optical properties and the meteorological conditions within the boundary layer during HPEs in Beijing. Our detailed conclusions are given in Section 4.

2. Data and Methods

2.1. Sun Photometer and LiDAR Measurements and Site Descriptions

We used the GQB I-03 atmospheric water vapor aerosol LiDAR at the CAMS observatory to obtain the vertical profiles of the optical properties of aerosols from September 2017 to February 2021. The instrument consists of six parts: a laser emission unit, a receiving telescope, a spectroscopic unit, a detector, an acquisition card and a control unit. The instrument emits a 532 nm wavelength laser and accepts 532 nm parallel and perpendicular and 607 and 660 nm Raman scattering signals. These signals are used to determine the physical properties of atmospheric aerosols, including the identification of non-spherical particles and the aerosol extinction coefficient, by detecting the scattering of the 532 nm laser using a polarization meter [56]. Raman-Mie LiDAR has a detection blind area of 200 m and a vertical resolution of 7.5 m. The aerosol extinction coefficient is retrieved using the algorithm of Fernald as follows, which considers the atmosphere to consist of air molecules and aerosols.

$$P(z) = CE[\beta_a(z) + \beta_m(z)]e^{-2\int_{z_0}^{z}[\alpha_a(z)+\alpha_m(z)]dz}$$

where P is the atmospheric backscattering echo power (W) at height z (km) received by LiDAR, C is the LiDAR system constant $\left(\mathrm{W{\cdot}km^3{\cdot}sr}\right)$, E is the LiDAR launch energy (μJ), β(z) is the backscattering coefficient $\left(\mathrm{km^{-1}{\cdot}sr^{-1}}\right)$ at height z (km), α(z) is the extinction coefficient $\left(\mathrm{km^{-1}}\right)$, a represents aerosols, and m represents air molecules.

Aerosol particles are not easily diffused vertically because the free atmosphere above the boundary layer is in a relatively static state. The aerosol concentration in the free atmosphere is therefore much lower than that in the boundary layer and the extinction coefficient decreases abruptly at a certain height with a gradient extreme, which we regard as the aerosol boundary layer height. We can obtain the aerosol boundary layer height by inversion of the vertical abrupt rate of change of the extinction coefficient. We use the aerosol boundary layer height to approximate the boundary layer height.

The sun photometer(CE-318, Cimel Electronique, Paris, France) is located on the roof of the CAMS building (at about 106 m above ground level) and was operated in February 2020 to obtain the aerosol optical depth (AOD) and the optical properties of the aerosols. The instrument has an uncertainty in cloud-screened AODs calculated by ASTPwin software(Cimel Electronique) were <0.01. It measures wavelengths of 340, 380, 440, 500, 670, 870, 1020 and 1640 nm and obtains the optical properties of aerosols from sky brightness and direct solar radiation measurements in the 440, 500, 670, 870, 1020 and 1640 nm channels, combined with direct solar AOD detection at the same wavelengths [13,14,22,57–59]. These inversion data include the coarse and fine mode aerosol volume concentrations, the Ångström exponent at 440–870 nm, the aerosol size distribution ($dV/dlnr$ in the range 0.05–15 μm), the single scattering albedo (SSA), the absorbing aerosol

optical depth (AAOD), the absorbing Ångström exponent (AAE) and the direct aerosol radiative forcing (DARF) [11,56,58–60]. The computational model of DARF is as follows:

$$DARF = \left(F^{\downarrow A} - F^{\uparrow A}\right) - \left(F^{\downarrow C} - F^{\uparrow C}\right)$$

$$DARF_{TOA} = \left(F_{TOA}^{\uparrow C} - F_{TOA}^{\uparrow A}\right)$$

$$DARF_{BOA} = \left(F_{BOA}^{\downarrow A} - F_{BOA}^{\downarrow C}\right)$$

$$DARF_{AH} = (DARF_{TOA} - DARF_{BOA})$$

Where F^A denotes the net radiative energy in the presence of aerosols, F^C denotes the net radiative energy in the absence of aerosols, and the arrows denote the direction of the global radiative flux, with downward fluxes denoted by ↓ and upward fluxes denoted by ↑, $DARF_{AH}$ is defined as the atmospheric heating term.

2.2. Meteorological and Pollutant Data

We used surface meteorological data from Haidian Station of the China Meteorological Administration, including the temperature, relative humidity, wind direction and wind speed (for location, see Figure 1). We obtained data on pollutants from the National Environmental Monitoring Center of China and used the arithmetic mean of 35 monitoring stations in Beijing to represent the overall air quality in Beijing [61]. Because Wanliu Station is close to the CAMS observatory (about 5 km), we used $PM_{2.5}$ data from Wanliu Station to represent the air quality in urban Beijing. The pollutant data included the hourly average data for $PM_{2.5}$, SO_2, NO_2 and CO, and the 8-h sliding average data for O_3.

We used daily sounding data at 08:00 and 20:00 from a sounding balloon at Beijing South Suburban Observatory (54511), including the pressure, temperature, temperature dew point difference, wind direction and wind speed. We obtained the convective available potential energy (CAPE) between 1000 and 100 hPa. When the CAPE is negative, it is expressed by the convective inhibition (CIN), which indicates that the lifting of pollutants is inhibited; dispersion will be strongly inhibited when the absolute value of CIN is >100 J kg^{-1} [62,63].

$$CAPE = R_d \int_{EL}^{LFC} T'_v - T_v d\ln p$$

where R_d is the dry gas constant (R_d = 287 J·$kg^{-1}K^{-1}$), p is the pressure and $T'_v - T_v$ is the difference between the virtual temperature of the micro-cluster of lifted air and the virtual temperature of the surrounding atmosphere. *LFC* is the level of free convection and *EL* is the equilibrium level [64].

The radar wind profiler deployed at Haidian Park (54399) provides the horizontal wind direction and speed and the vertical velocity below about 3 km above the ground with a vertical resolution of 120 m and a temporal resolution of 6 min, measured from 150 m [65,66]. We explored the interactions between the wind field and changes in the concentration of pollutant during HPEs.

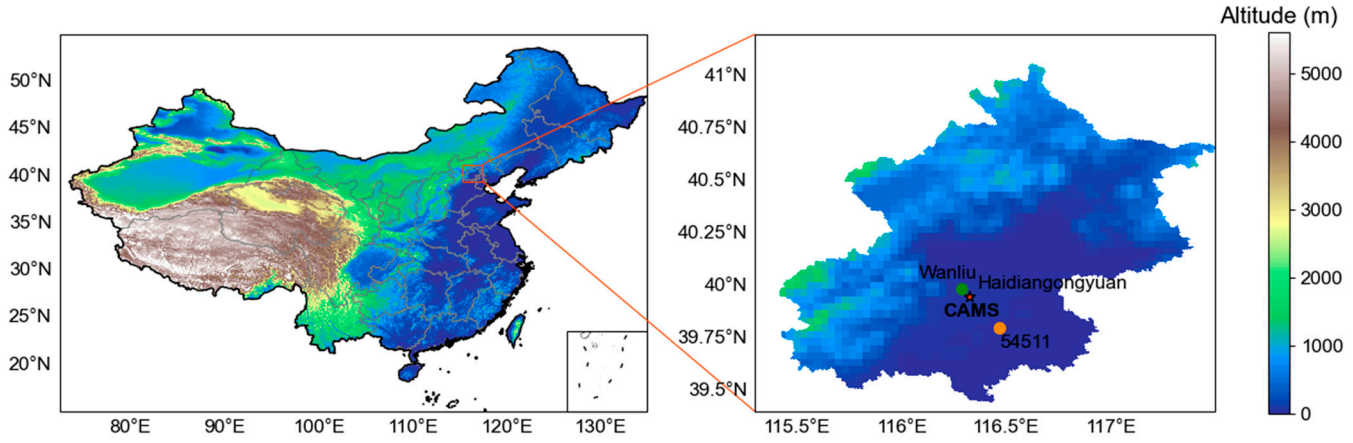

Figure 1. Location of the meteorological stations in Beijing. Red star, CAMS; orange dot, Beijing South Suburban Observatory (54511); and green dot, Haidian Park (54399) and Wanliu Station.

3. Results and Discussion

3.1. Climatological Characteristics of the Vertical Distribution of Aerosols

As an important parameter of the aerosol extinction capacity, the extinction coefficient reflects the aerosol load in the atmosphere, whereas the aerosol vertical profile reflects the vertical distribution of aerosols [67]. Figure 2 shows the characteristics of the inter-month variation of the atmospheric extinction coefficient in urban Beijing from autumn 2017 to winter 2020. The area with the maximum change in the vertical profile of the extinction coefficient in all months is concentrated within 2 km above ground level (monthly average value of the extinction coefficient >0.1 km^{-1}). The aerosol extinction coefficient decreases with increasing height, which suggests that the concentration of atmospheric aerosols in urban Beijing is highest near ground level [67].

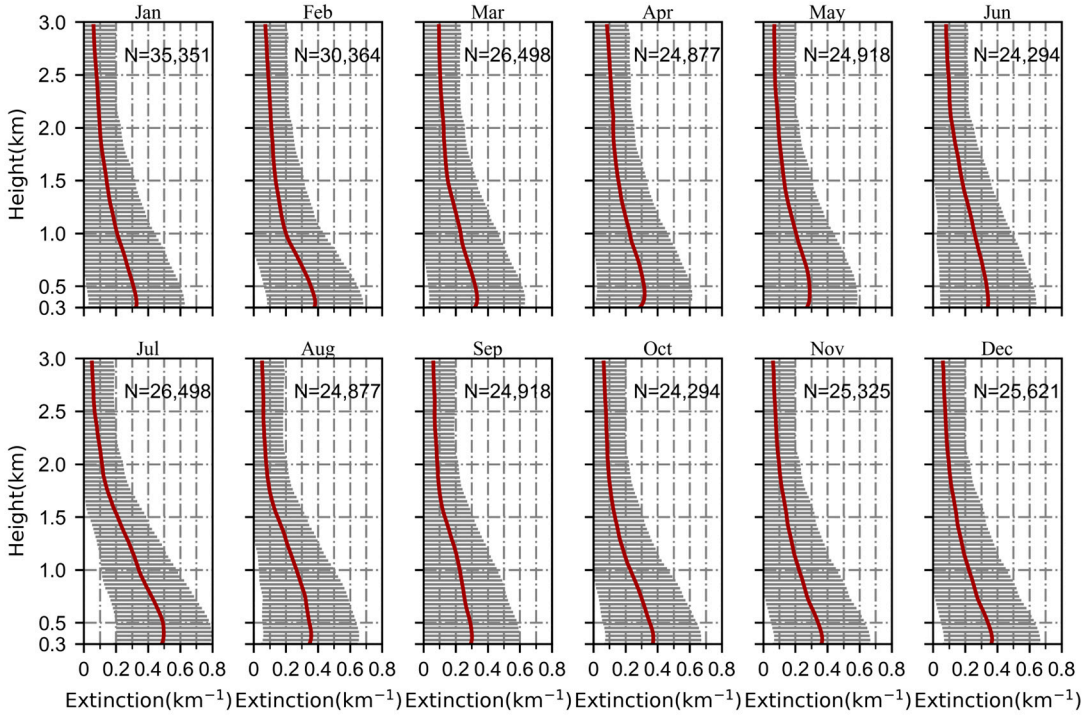

Figure 2. Vertical profiles of the monthly average change in the aerosol extinction coefficient in urban Beijing from September 2017 to February 2021, and the error bars (gray) are standard deviations. Where N denotes the total number of aerosol extinction profiles for each month.

The extinction coefficient is largest in summer, followed by winter, and is roughly the same in both spring and autumn, with mean values of the extinction coefficient at 300 m being about 0.4, 0.35 and 0.3 km^{-1}. The aerosol extinction coefficient within 2 km of ground level is highest in summer, especially in July, and the extinction coefficient at 300 m is 0.5 km^{-1}. This suggests that aerosol particles are more likely to absorb moisture and grow under the high temperature and high humidity conditions in summer, increasing the extinction coefficient [68–70]. It also suggests that there is a broader distribution of aerosol particles in summer. This may be because the maximum height of the boundary layer in summer can develop to about 2 km and aerosol particles are transported to this altitude via turbulence [71,72]. The extinction coefficient within 0.5 km of the ground is also relatively large in February, October, November and December, with an average value of about 0.4 km^{-1}. This is because buildings in Beijing are heated during autumn and winter, leading to higher emissions of pollutants, more frequent pollution events and higher aerosol mass concentrations, resulting in an increase in the extinction coefficient within 0.5 km of the ground surface [25].

In the range 1–2 km above ground level, the extinction coefficient is highest in summer, followed by spring and autumn, and smallest in winter. The extinction coefficient in the range 1–2 km varies between 0.1 and 0.2 km^{-1} in winter because the mean value of the boundary layer height is <1 km in this season [72,73] and aerosol particles are not easily transported to >1 km, resulting in a smaller extinction coefficient for aerosols above 1 km. Aerosols are transported to high altitudes during the frequent dust events in Beijing in spring [74–76] and the extinction coefficient is therefore largest at 2–3 km in spring. The mean value of the extinction coefficient is about 0.1 km^{-1} and it is almost unchanged with increasing height.

Figure 3 shows the daily variation of the atmospheric extinction coefficient in urban Beijing from autumn 2017 to winter 2020. In spring, turbulent motion transports aerosol particles to 0.5–1 km during the development of the boundary layer from 07:00 and the aerosol extinction coefficient gradually increases in this height range until reaching a maximum value around noon. The aerosol extinction coefficient within about 0.75 km is >0.3 km^{-1}. The height of the boundary layer decreases from 12:00 to 23:00 and from 00:00 to 06:00 and the aerosol particles are gradually pressed downward to below 0.5 km. The extinction coefficient of aerosols at 2–3 km altitude in spring is higher from 02:00 to 14:00 than in other seasons as a result of the frequent occurrence of sand and dust pollution in Beijing [74–76].

In summer, the boundary layer develops at 07:00 and turbulent motion brings aerosols from below 0.5 km to between 0.5 and 1.5 km. The extinction coefficient between 0.5 and 1.5 km gradually increases until it reaches a maximum at 13:00. The extinction coefficients are all >0.3 km^{-1} within about 1.25 km of the ground surface. Between 13:00 and 18:00, as the sun sets, the aerosols in the range 0.5–1.5 km above the ground surface are gradually depressed to below 0.7 km, the extinction coefficient within the range 0.5–1.5 km decreases, and the lowest extinction coefficient gradually increases to 0.45 km^{-1}. However, in the range 1–1.5 km, the extinction coefficient always remains between 0.15 and 0.3 km^{-1} because some aerosols are retained in the residual layer, resulting in a relatively high extinction coefficient between 1 and 1.5 km [77,78].

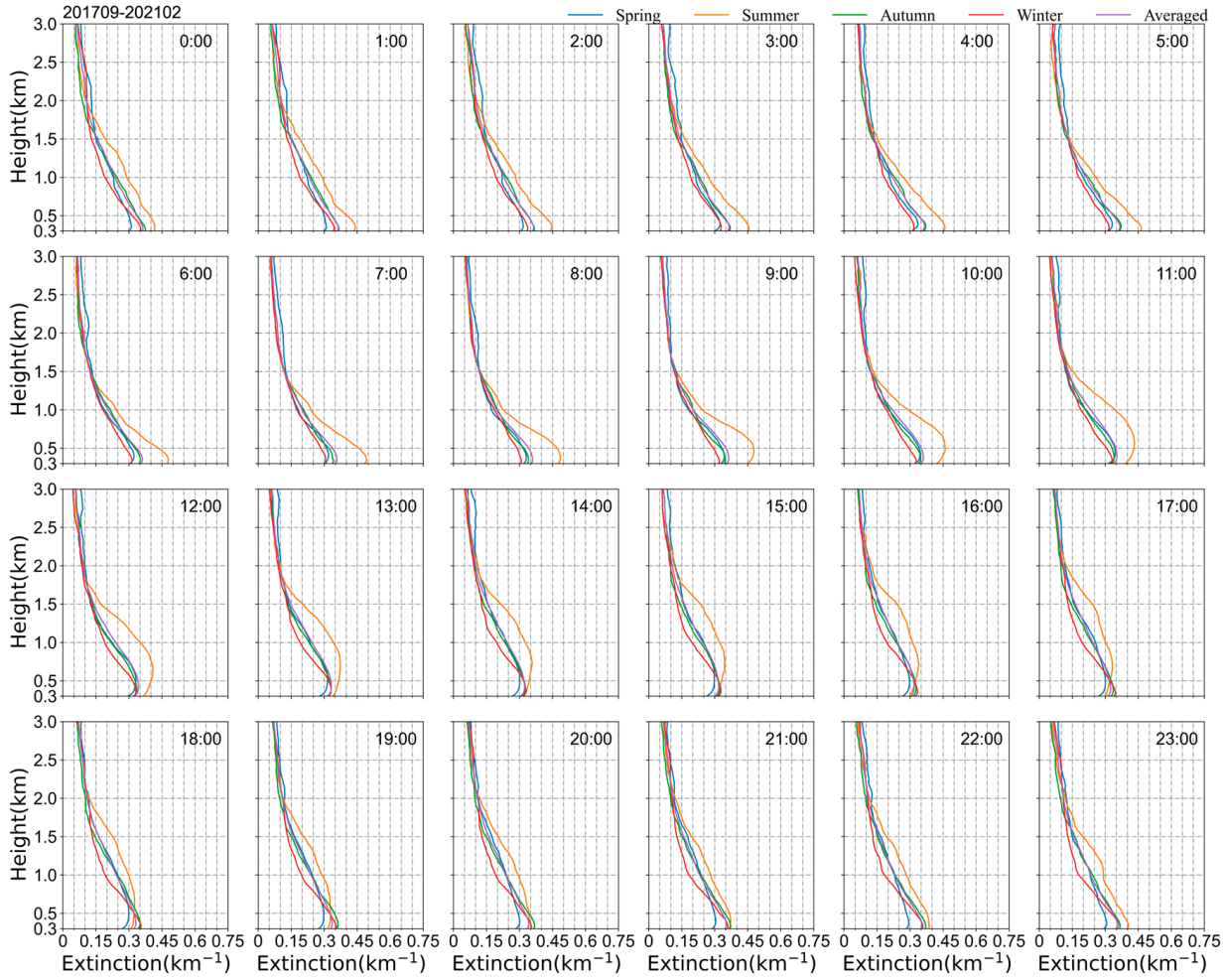

Figure 3. Hourly variations in the vertical profile of the aerosol extinction coefficient in urban Beijing from September 2017 to February 2021.

The daily variation in the vertical distribution of aerosols in autumn is similar to that in spring. In winter, with the development of the boundary layer from 08:00 to 14:00, the aerosol extinction coefficient between 0.5 and 1 km gradually increases and the aerosol extinction coefficient below about 0.6 km is >0.3 km^{-1}. The boundary layer height decreases after 14:00 and the aerosol particles are gradually pressed down to below 0.5 km. From 12:00 to 18:00, the aerosol extinction coefficient in the range 0.5–2 km is significantly lower in winter than in other seasons. By contrast, the aerosol extinction coefficient below 0.5 km is higher than in other seasons. This is because the boundary layer height is relatively low in winter and pollutants are not easily transported to altitudes >0.5 km [72]. In addition, winter is the main heating season in Beijing and the emission of pollutants increases the aerosol extinction coefficient below 0.5 km [25].

3.2. Case Study of Haze Pollution from 8 to 15 February 2020

We investigated the effects of the vertical motion of the boundary layer on particulate matter and its optical properties during an extreme haze event and the link between the vertical distribution of aerosols and the meteorological conditions within the boundary layer. Based on observations from the Raman–Mie scattering LiDAR and sun photometer combined with meteorological data, we conducted a comprehensive analysis of an extreme haze event in Beijing from 8 to 15 February 2020.

3.2.1. Meteorological Conditions within the Boundary Layer

Figure 4 shows the variation of the $PM_{2.5}$ mass concentration, the Ångström exponent at 440–870 nm ($AE_{440–870nm}$), the AOD, the boundary layer height, the temperature, the relative humidity, the wind direction and the wind speed in urban Beijing from 8 to 15 February 2020. Figure 4a shows that a heavy pollution event occurred in Beijing from February 8 to 15. Pollutants began to accumulate from about midnight on February 8, when the $PM_{2.5}$ mass concentration increased suddenly from 15 to 180 μg m^{-3} and then remained steady at about 120 μg m^{-3}. The concentration of pollutants increased suddenly from about 09:00 to 12:00 on 11 February, when the $PM_{2.5}$ mass concentration increased from 120 to 250 μg m^{-3}, after which it remained at around 240 μg m^{-3}. Precipitation occurred in the Beijing area from the afternoon of 13 February to 14 February and the pollutants gradually cleared via wet deposition. The $PM_{2.5}$ mass concentration decreased and the pollution event ended. We focus here on two cumulative growth processes of pollutants: from 12:00 on 8 February to 01:00 on 9 February (PE1) and from 18:00 on 10 February to 18:00 on 11 February (PE2). We analyzed the influence of the vertical motion of the boundary layer on particulate matter and its optical properties during HPEs and the connection between the vertical distribution of aerosols and the meteorological conditions within the boundary layer.

Figure 4 shows that the near-surface wind speed was low in PE1 and mainly dominated by westerly and easterly winds. The $PM_{2.5}$ mass concentration increased rapidly from 15 to 180 μg m^{-3} and the AOD showed an increasing trend similar to that of $PM_{2.5}$. The boundary layer height showed a fluctuating decreasing trend, which was influenced by the combined effect of the daily variation in the boundary layer and the aerosol radiation effect [21]. The near-surface temperature had a clear daily trend, with the minimum temperature increasing from −9 to −3 °C at the beginning of the period of relative pollution, indicating that the presence of an aerosol particle layer at night enhances the downward counter-radiation in the atmosphere and heats the underlying atmosphere, increasing the daily minimum temperature [79].

The changes in the relative humidity and $PM_{2.5}$ both showed an increasing trend. The change in the relative humidity was influenced by the daily change in the water vapor content and temperature [80]. Before sunset, the amount of shortwave radiation reaching the near-surface decreased as a result of aerosol extinction [21]. The near-surface region therefore cooled down, the saturated water vapor pressure decreased and the relative humidity gradually increased [80]. After sunset, the temperature near the ground gradually decreased and therefore the saturated water vapor pressure also decreased, resulting in a gradual increase in the relative humidity [80].

In PE2, the near-surface region was in a static state with a wind speed <2 m s^{-1}. The temperature and relative humidity showed clear daily variations, but the minimum value of the relative humidity increased from 30% on 10 February to about 45% on 11 February and the maximum temperature decreased from 13 to about 11 °C. This suggests that the amount of solar radiation reaching the near-surface decreased as a result of the extinction effect of pollutants, which led to a decrease in the near-surface temperature and an increase in the relative humidity [50,51].

The $PM_{2.5}$ mass concentration increased rapidly from 120 μg m^{-3} to about 250 μg m^{-3} at 09:00–12:00 on 11 February, whereas the boundary layer height decreased from 1.1 to about 0.6 km. This was caused by the accumulation of pollutants leading to radiative cooling near the ground, lowering the surface temperature and forming or enhancing the inverse temperature lamination. This inhibited the diffusion of vertical turbulence and led to a decrease in the boundary layer height [54,55].

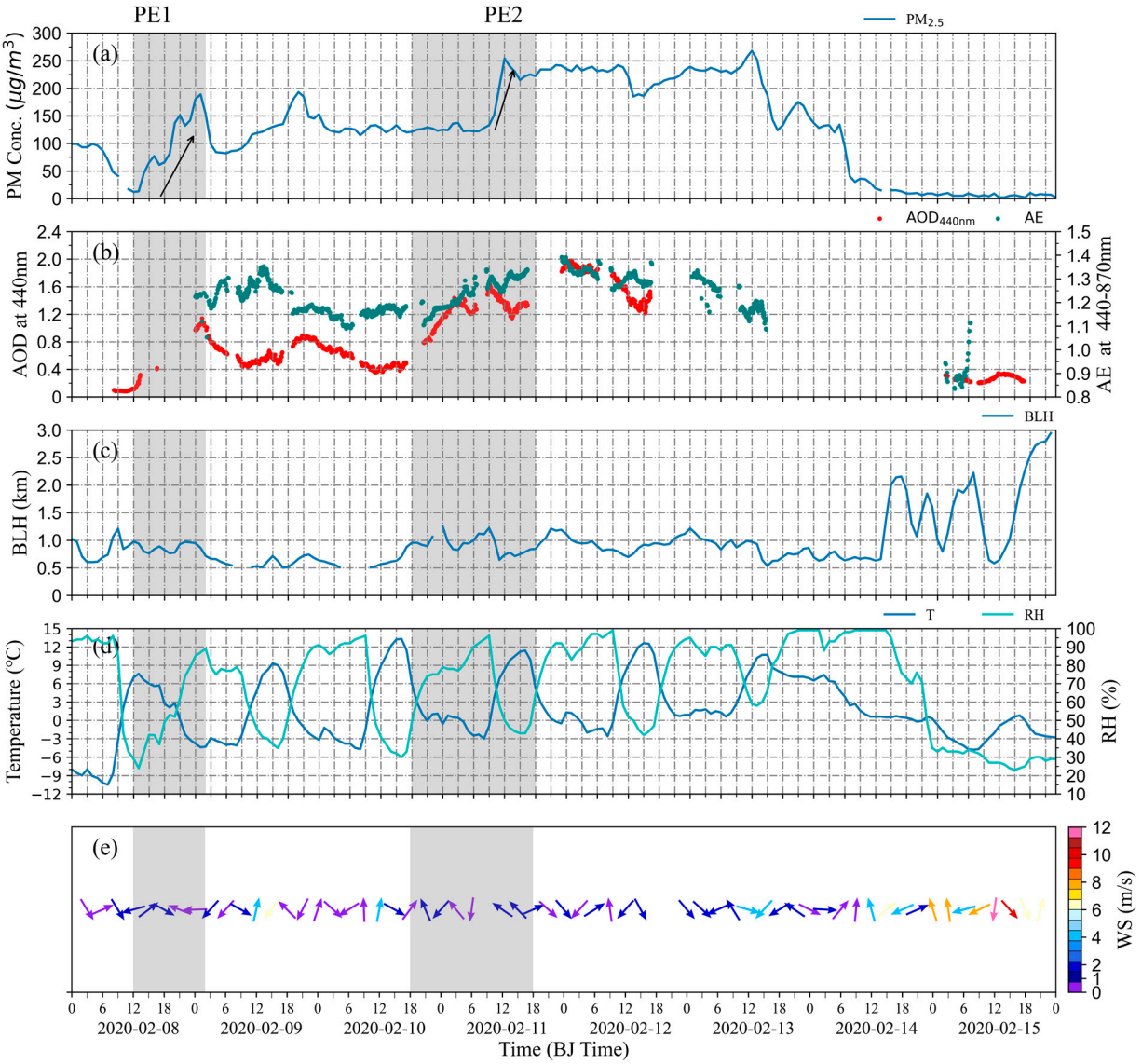

Figure 4. Time series of (**a**) the $PM_{2.5}$ mass concentration, (**b**) the aerosol optical depth (AOD) and Ångström exponent ($AE_{440–870nm}$), (**c**) the boundary layer height (BLH), (**d**) the temperature (T) and relative humidity (RH) and (**e**) the wind direction (WD) and wind speed (WS). The arrows indicate explosive increase in PM mass concentration.

The AOD_{440nm} increased from 0.4 to 1.6 from about 18:00 on 10 February to 08:00 on 11 February, whereas the Ångström exponent increased from 1.2 to 1.6, indicating that the accumulation of pollutants during PE2 was dominated by fine particles [14]. The increasing trends presented by both $PM_{2.5}$ and AOD_{440nm} were not synchronized in time. The $PM_{2.5}$ mass concentration increased about 2.1 times from 09:00 (about 120 μg m^{-3}) to 12:00 (about 250 μg m^{-3}) on 11 February, whereas the AOD_{440nm} increased about four times from 18:00 (about 0.4) on 10 February to 09:00 (about 1.6) on 11 February (Figure 4). Figure 4 shows that the increase in the AOD was synchronized with the increase in the relative humidity. The increase in the AOD may be because, at high particle concentrations (about 120 μg m^{-3}), the hygroscopic growth of a large number of fine particles with increasing relative humidity increases the scattering of particles [32].

The increases in the SSA at 675, 870 and 1020 nm all showed different degrees of growth. The vertical profile of the extinction coefficient also showed different degrees of growth at each height, especially at the lowest layer, where there was an increase of about 3.3 times from 0.6 to 2.0 (Figure S1). This led to a decrease in the amount of radiation reaching the

near-surface and an increase in the amount of radiation trapped in the boundary layer. This strengthened the inversion layer in the boundary layer and suppressed the development of turbulence. The height of the boundary layer decreased from 1.1 to 0.6 km from 09:00 to 12:00 on 11 February (Figure 4). Particulate matter accumulated continuously from high altitudes to the near-surface, which promoted the rapid growth in the mass concentration of $PM_{2.5}$.

The vertical transport of particulate matter may also explain the lack of synchronization in the incremental trends presented by the AOD_{440nm} and the $PM_{2.5}$ mass concentration. The $PM_{2.5}$ mass concentration is measured with the micro-oscillation balance and β-absorption methods [81], which respond to the near-surface mass concentration of $PM_{2.5}$, whereas the AOD reflects the whole aerosol column [21]. The pollutants may be suspended in the atmosphere, resulting in low $PM_{2.5}$ mass concentrations from near-surface observations, while the AOD shows an increasing trend.

Figure S1 shows that the aerosol extinction coefficient at 1–1.5 km continued to grow from 18:00 on February 10 to about 10:00 on 11 February. The aerosol extinction coefficient increased from about 0.1 to 0.3 km^{-1} at 1 km height and the high-value region of the aerosol extinction coefficient (>0.3 km^{-1}) gradually thickened from <1 km to about 1.25 km, indicating the continuous accumulation of pollutants between 1 and 1.5 km. At the height of 1000 hPa, the Beijing area was located on the eastern side of a region of high pressure system and the near-surface winds were mainly northerly. With an eastward shift in the region of high pressure, the wind speed gradually decreased at the near-surface and was relatively stable, and the strengthening of the sinking airflow in Beijing. From 00:03 to 12:00 on 11 February, there was a sinking airflow with a wind speed of about 0.5 m s^{-1} between 0 and 1.5 km, which continuously transported pollutants from altitudes of 1–1.5 km to the near-surface. This promoted the rapid increase in pollutants.

Figure 5 shows the contribution of CAPE to the variation in the $PM_{2.5}$ concentration. When the CAPE is negative, the diffusion of pollutants is inhibited and is expressed by the CIN [62,63]. During PE1 and PE2, the atmosphere had a stable stratification at 08:00 and 20:00 and the diffusion of pollutants was inhibited. The temperature within the boundary layer (1000–900 hPa) gradually increased with height during PE2 at 08:00 and 20:00 on 10–11 February, showing an inverse temperature stratification. This further enhanced the accumulation of pollutants.

The wind field is an important meteorological factor affecting the accumulation or dispersion of atmospheric pollutants [66]. Figures 6 and 7 show the horizontal wind field profiles and vertical wind field plots, respectively, during this period of haze pollution. Positive values in the vertical wind field plots indicate a sinking airflow and negative values indicate a rising airflow. During PE1, Beijing was in the southeast of the low-pressure system from 12:00 to 18:00 and the near-surface winds were mainly southerly. Pollutants were continuously transported from southern Beijing to downtown Beijing, which accelerated the accumulation of pollutants [50]. With the eastward movement of the low-pressure system, the near-surface wind speed weakened and the lifting airflow gradually strengthened.

During PE2, the Beijing area was located on the eastern side of the high-pressure region and the near-surface winds were mainly northerly. The near-surface wind speed decreased with the eastward shift in the high-pressure region and the sinking airflow was enhanced. At around 12:00 to 18:00 on 11 February, a sinking airflow with wind speeds of 1.5–2.5 m s^{-1} appeared below 500 m, which transported pollutants to the near-surface and promoted their accumulation, leading to a stable $PM_{2.5}$ mass concentration of about 250 μg m^{-3} (Figure 4).

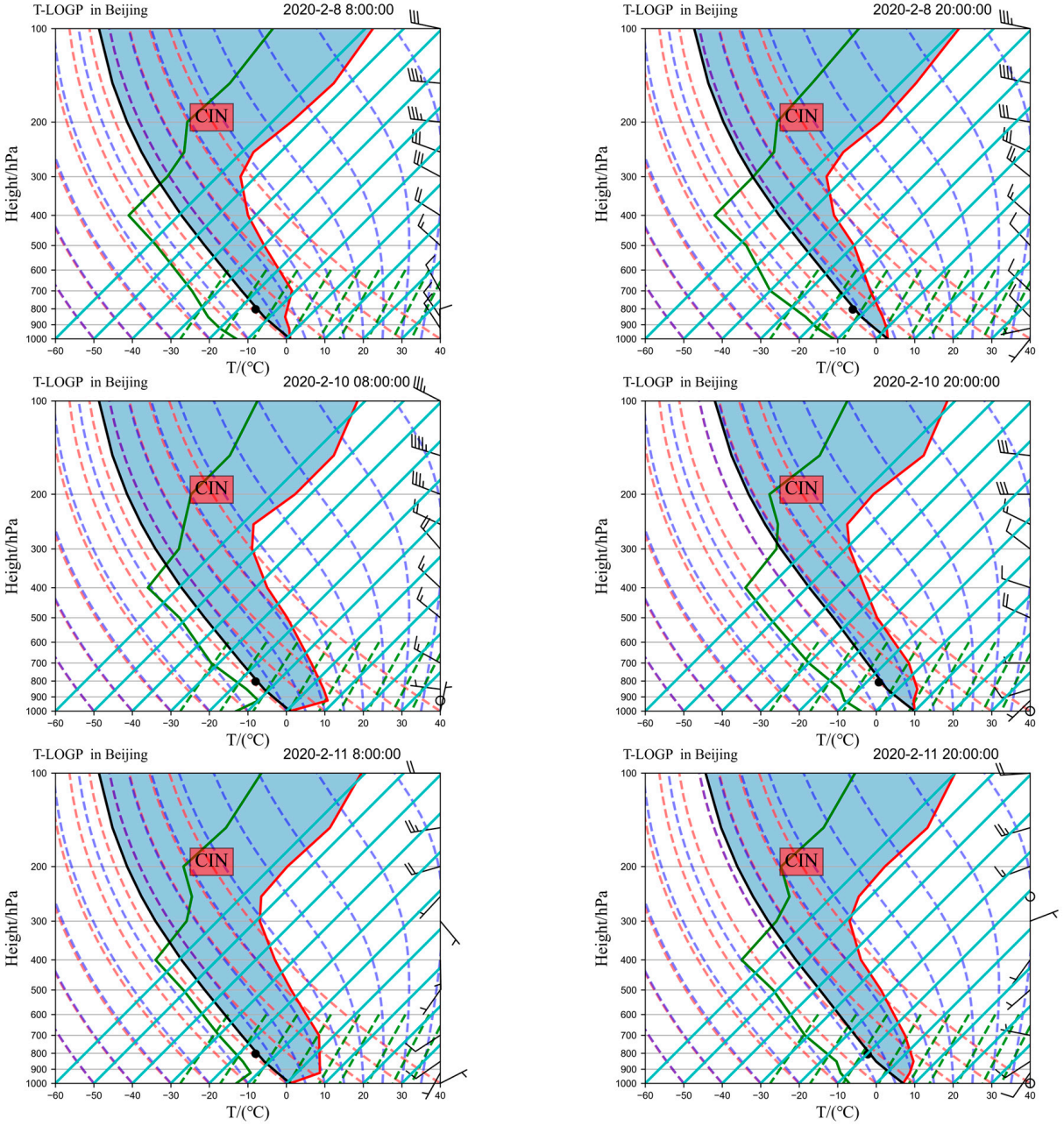

Figure 5. Temperature (T)—pressure (lnP) plots in urban Beijing at 08:00 and 20:00 on 8, 10 and 11 February 2020. The solid gray line shows the isobaric pressure line, the solid cyan line is the isothermal line, the solid green line is the vertical profile of ambient temperature, the solid red line is the vertical profile of ambient dew point, the solid black line is the adiabatic lift path of the gas mass, the dashed red line is the dry adiabatic line, the dashed blue line is the wet adiabatic line, and the dashed cyan line is the isosaturated specific humidity line.

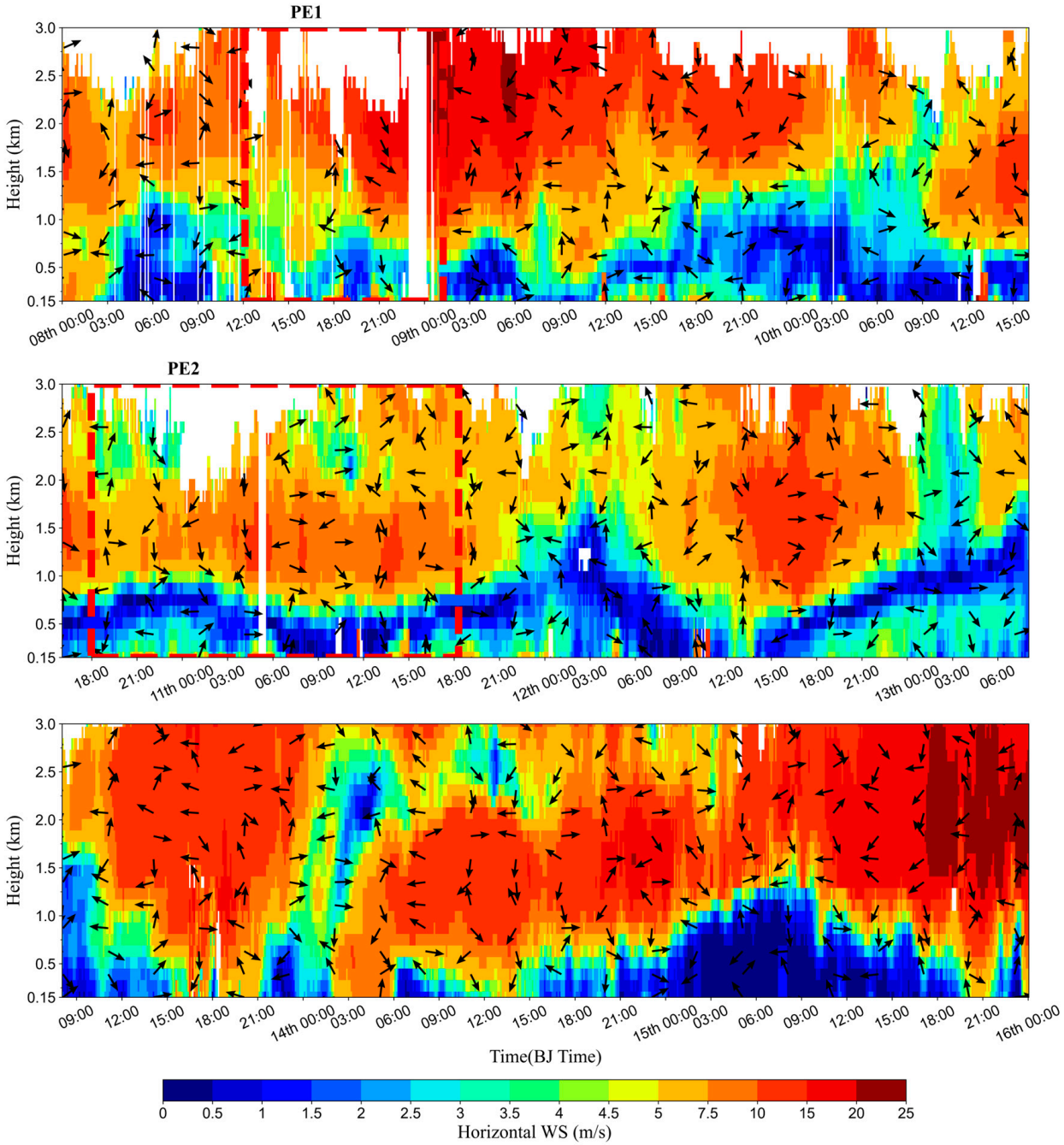

Figure 6. Horizontal wind speed (WS) in urban Beijing from 8 to 15 February 2020. Arrows indicate the wind direction.

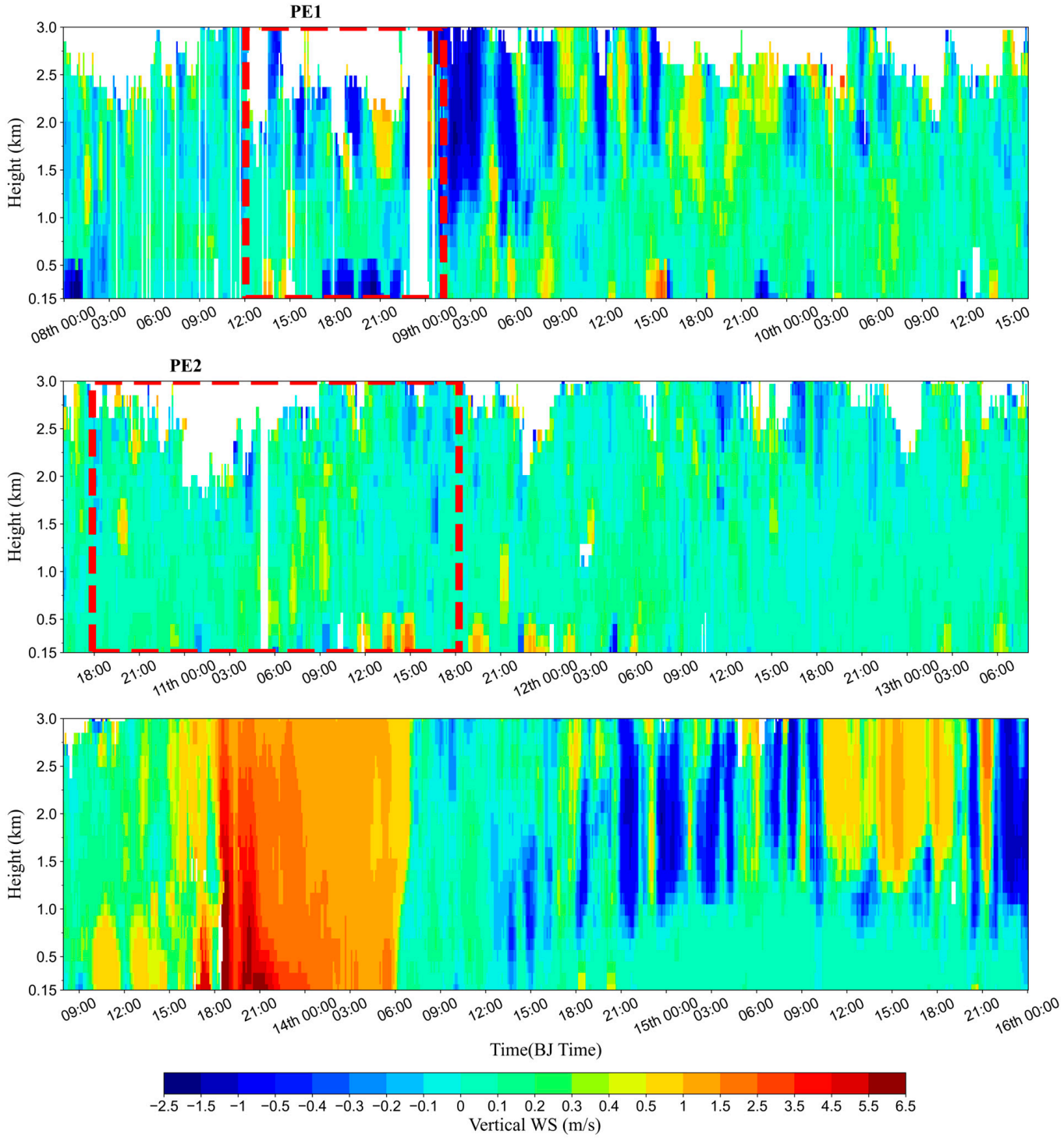

Figure 7. Vertical winds in urban Beijing from 8 to 15 February 2020. Positive values indicate downdrafts and negative values indicate updrafts.

3.2.2. Aerosol Optical Properties

Figure 8 shows the spatiotemporal distribution of the extinction coefficient and depolarization ratio of aerosols below 3 km from 8 to 15 February 2020. In general, aerosols, sea salt particles and the water droplets in clouds are almost spherical, with a relatively low depolarization, so they are not easily distinguished from atmospheric pollutants. By contrast, dust aerosols and ice crystals in ice clouds are non-spherical with a relatively large depolarization (>0.2), so they are easily distinguished from atmospheric pollutants [74].

Figure 8 shows that the polluted aerosol layer during this haze was mainly concentrated within 1 km and the depolarization ratio was <0.2. In PE1, the pollutants started to accumulate from about 13:00 on 8 February and the aerosol extinction coefficient gradually increased significantly from <0.1 to 1.3 km^{-1} within 1 km. The aerosol concentration increased significantly and the depolarization ratio was <0.2 during the accumulation of pollutants, indicating that this process consisted mainly of the accumulation of spherical particles. In PE2, with the accumulation of pollutants, the height of the area with a high aerosol extinction coefficient gradually increased to about 1.0 km and the receding polarization ratio of this layer was relatively large (>0.2) from 12:00 to 18:00 on 10 February. There was an updraft of 1–1.5 m s^{-1} below 500 m at about 12:00 on 10 February (Figure 7). This indicates that a dust-raising process that produced non-spherical particles occurred from 12:00 to 18:00. The receding polarization ratios were relatively low (<0.1) at all other times, indicating that a large number of water-soluble spherical particles were produced during this haze episode [21].

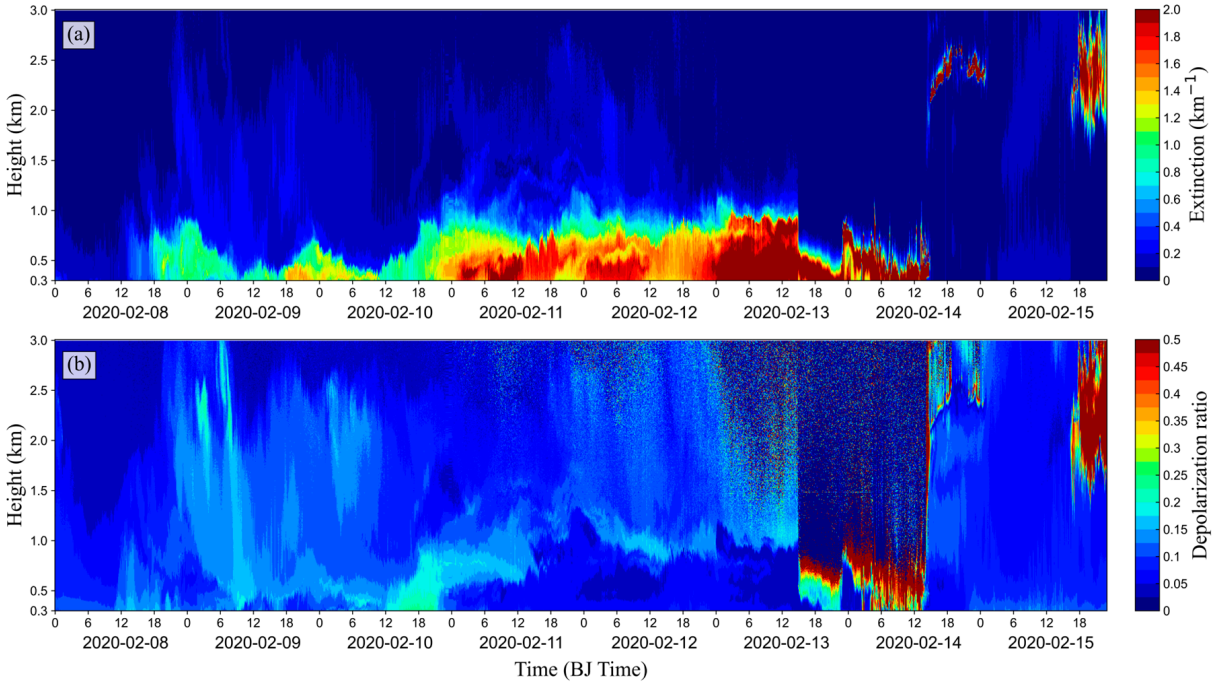

Figure 8. Spatial and temporal distribution of the extinction coefficient (**a**) and depolarization ratio (**b**) in urban Beijing from 8 to 15 February 2020.

Figure 9 shows the trends of the SSA, AAOD, AAE, DARF, the volume distribution of coarse and fine particles, and the volume spectrum distribution of aerosols throughout the pollution process. The SSA440nm was between 0.95 and 0.975 throughout the heavy pollution event, indicating that scattering aerosol particles were predominant throughout. This may be because, under high relative humidity (daily average > 65%), a large number of fine modal particles absorb moisture and grow, thus increasing the scattering of aerosols [32]. SSA1020nm, SSA870nm, SSA675nm and SSA440nm gradually converged with the accumulation of pollutants, indicating that the scattering of each band was greatly increased as the pollutants accumulated.

The AAE is often considered to be a key factor in determining the types of particles absorbing radiation (e.g., black carbon, organic materials or mineral dust) [82]. Specifically, the AAE of mixtures of black carbon with organic or inorganic components is <1, the AAE of the black carbon emitted from the combustion of fossil fuels is roughly equal to 1, and the AAE of black carbon and mineral dust emitted from the combustion of biomass is roughly equal to 1.1 [21]. The AAOD in all four bands (440, 675, 870 and 1020 nm) showed

an increasing trend with the accumulation of pollutants, especially from 10 to 11 February, when the $AAOD_{440nm}$ increased from 0.016 to 0.054 and the AAE increased from 0.62 to 1.21. This indicates that the dust present on 10 February (Figure 8) was an important factor in enhancing absorption by aerosols [23].

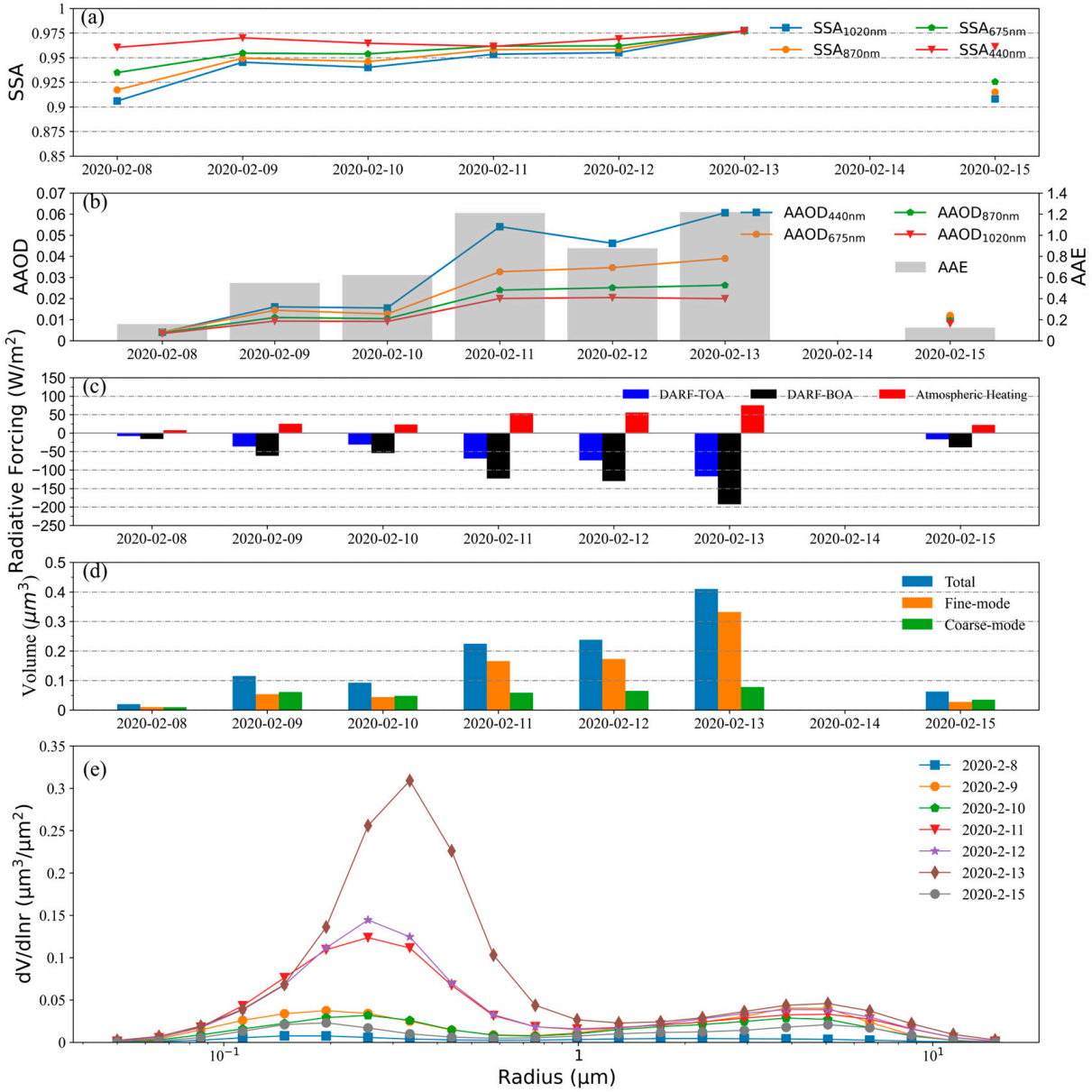

Figure 9. (**a**) The single scattering albedo (SSA), (**b**) the absorbing aerosol optical depth (AAOD) and absorbing Ångström exponent (AAE), (**c**) the direct aerosol radiative forcing (DARF), (**d**) the volume distribution of coarse and fine particles and (**e**) the spectral distribution of the aerosol volume (dV/dln(r)) for the period from 8 February to 15 February 2020 in urban Beijing.

The particle spectrum of the aerosol volume concentration showed a bimodal logarithmic distribution throughout the pollution process. The volume of fine modal particles increased gradually with the accumulation of pollutants and the peak concentration increased from 0.008 to 0.31 $\mu m^3\ \mu m^{-2}$. The total volume increased from 0.01 to 0.33 μm^3, whereas the total volume of coarse modal particles increased from 0.009 to 0.061 μm^3 on 8–9 February, but then did not change much. This suggests that the aerosol particles accumulated throughout the pollution process, whereas some coarse modal particles accumulated

on 8–9 February. As the volume of fine modal particles increased, their peak concentration and the radius of fine particles corresponding to the peak concentration also increased. For example, the peak concentration of fine modal particles on 10 February was 0.03 μm^3 μm^{-2} and the radius was 0.25 μm. However, as the pollutants accumulated, by 13 February the peak concentration of fine modal particles was 0.31 μm^3 μm^{-2} and their radius was 0.33 μm. This may be due to the accumulation of a large number of water-soluble particles (e.g., sulfate and nitrate particles) during the accumulation of pollutants. The hygroscopic growth of these particles at high relative humidity (daily average > 65%) results in a gradual increase in the size of fine particles as pollutants accumulate [83].

Figure 9 shows that the volume of both coarse and fine mode particles increased significantly on 8–9 February. The volume of fine mode particles increased from 0.01 to 0.054 μm^3 and the volume of coarse mode particles increased from 0.009 to 0.061 μm^3. The peak volume concentration of fine mode particles on 9 February was 0.037 μm^3 μm^{-2}, which corresponds to a radius of 0.2 μm for fine mode particles. The peak volume concentration of coarse mode particles was 0.04 μm^3 μm^{-2} with a radius of 3.9 μm, which indicates that both coarse and fine particles accumulated considerably during the accumulation phase on 8 and 9 February.

The SSA440nm increased slightly from 0.96 to 0.97, whereas the SSA increased substantially at 670–1020 nm, which may be due to its dependence on wavelength. The $AAOD_{440nm}$ increased from 0.004 to 0.016 and the AAE increased from 0.15 to 0.56. This indicates that a mixture of black carbon and organic or inorganic components may have been present in the pollutants during this accumulation stage, resulting in enhanced absorption [84]. As the aerosol mass concentration increased, direct radiative forcing also increased to varying degrees, with the DARF at the base of the atmosphere decreasing from −15.7 to −61.5 W m^{-2}, suggesting that aerosol extinction greatly reduced the solar energy received at the Earth's surface [21].

Figure 9 shows that the volume of fine mode particles increased significantly on 10–13 February, with the volume of fine mode particles increasing from 0.044 to 0.332 μm^3. By contrast, the volume of coarse mode particles did not increase significantly compared with that on 8–9 February, which indicates that the aerosol particles accumulated in PE2 were mainly fine mode particles. The peak concentration of the volume of fine mode particles on 13 February was 0.31 μm^3 μm^{-2} and the corresponding radius was 0.33 μm. The SSA440nm increased from about 0.96 to about 0.98, whereas the SSA670–1020nm gradually converged with the SSA440nm, indicating that the scattering of each band was greatly increased with the accumulation of pollutants. The increase in the $AAOD_{440nm}$ from 0.016 to 0.061 and the AAE from 0.62 to 1.2 suggests the accumulation of black carbon or mineral dust aerosols from the burning of biomass in the PE2 phase. This can be explained by dust lifting from the surface on 10 February. The heating capacity of the atmosphere increased about 3.2 times from 10 February (23.2 W m^{-2}) to 13 February (75.5 W m^{-2}) as a result of the strong absorption of mineral dust aerosols.

3.3. Characteristics of Changes in Aerosol Precursors

The concentrations of CO are mainly influenced by the primary sources and the meteorological conditions, whereas $PM_{2.5}$ is also influenced by secondary sources [85,86]. CO can therefore be used to normalize the $PM_{2.5}$ concentrations to exclude the effects of primary emissions and meteorological conditions. We qualitatively assessed the intensity of secondary transformations in $PM_{2.5}$ using the $PM_{2.5}$/CO ratio (Figure 10) [81,85,87]. On 15 February (clean day), the daily average relative humidity was about 29% and the $PM_{2.5}$/CO ratio was low, with a mean value of 30.8×10^{-3} and a maximum value of 42.1×10^{-3}. On February 13, when the pollution was higher, the daily average relative humidity was about 84% and the $PM_{2.5}$/CO ratio had an average value of 95.0×10^{-3}, about 3.1 times higher than that on February 15. Comparing the $PM_{2.5}$/CO values on 13 and 15 February showed that secondary particulate matter was easily generated under conditions of high relative humidity [88–90].

The daily mean $PM_{2.5}$/CO values showed a fluctuating increasing trend as the pollution developed from 8 to 13 February. The daily mean $PM_{2.5}$/CO values increased about 1.3 times from the early (68.3×10^{-3}) to late (95.0×10^{-3}) stages of the pollution event. This indicates that secondary transformation intensified when the pollution accumulated in the late stage [87]. During PE1, the $PM_{2.5}$/CO ratio increased from about 40.0×10^{-3} to about 120.0×10^{-3}, indicating that secondary transformation was gradually increasing during PE1. CO, NO_2 and O_3 all increased with the $PM_{2.5}$/CO ratio, but the SO_2 concentration did not change significantly and the incremental increase in the SSA (Figure 9) on 8–9 February was probably due to secondary sulfate. As the accumulation of pollutants increased [87], a large amount of SO_2 was converted to $SO_4{}^{2-}$. In PE2, the $PM_{2.5}$/CO ratio showed a decreasing trend from about 100×10^{-3} to 80.0×10^{-3}. The CO and SO_2 concentrations showed a clear increase, whereas O_3 showed clear daily variations, indicating that the role of secondary conversion gradually decreased. The SSA also appeared to increase and NO_2 may have been converted to $NO_3{}^{-}$.

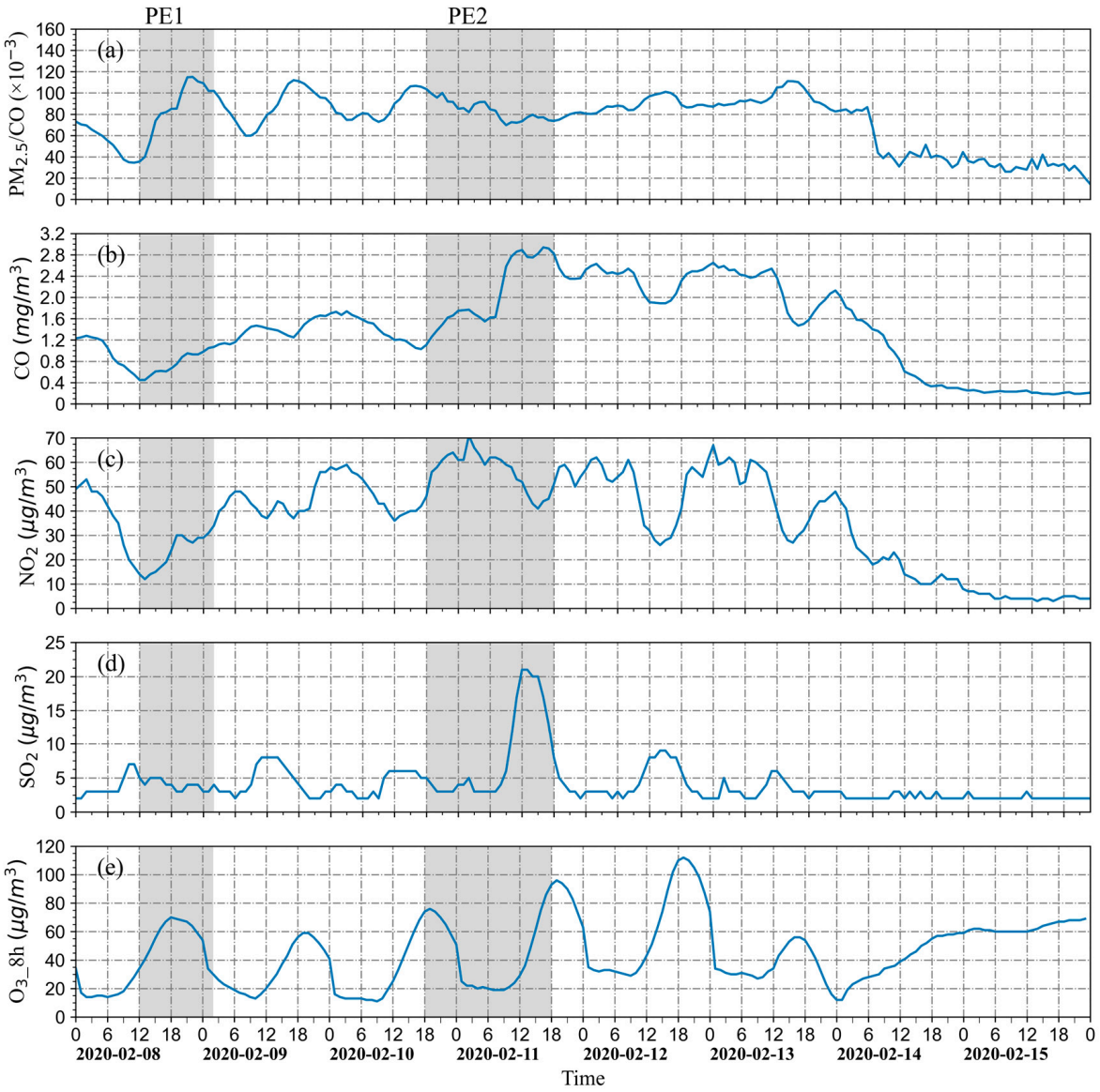

Figure 10. Changes in the mass concentrations of near-surface pollutants in Beijing from 8 to 15 February 2020. (**a**) $PM_{2.5}$/CO, (**b**) CO, (**c**) NO_2, (**d**) SO_2 and (**e**) O_3 (the ozone concentrations are 8-h sliding averages).

4. Conclusions

We have studied the vertical distribution of aerosols over Beijing from 2017 to 2021 based on long-term LiDAR observations. We have analyzed the influence of the vertical distribution of aerosols and their interconnection with the meteorological conditions within the boundary layer during an episode of heavy haze pollution in Beijing from 8 to 15 February 2020.

The vertical profile of the aerosol extinction coefficient was different in different seasons and at different altitudes. Below 2 km, the aerosol extinction coefficient was highest in summer, lower in winter, and lowest in spring and autumn; the lowest extinction coefficients were about 0.4, 0.35 and 0.3 km^{-1}, respectively. The maximum height of the boundary layer in Beijing can reach about 2 km in the summer months. Aerosol particles can be transported to an altitude of about 2 km via turbulence and the high relative humidity in summer makes it easier for aerosol particles to absorb moisture and grow, resulting in the high aerosol extinction coefficient below 2 km in summer. At the upper level of 2–3 km, the aerosol extinction coefficient was highest (about 0.1 km^{-1}) in spring and roughly comparable in summer, autumn and winter (<0.1 km^{-1}). This is due to the frequent occurrence of dust pollution events in Beijing in spring and the transport of dust aerosols to an altitude of 2–3 km. This leads to a larger aerosol extinction coefficient that does not change with height.

The vertical profile of the aerosol extinction coefficient showed a clear daily variation in all four seasons. The development of the boundary layer and the vertical distribution of aerosols were different in different seasons. The height of the high-value zone of the aerosol extinction coefficient was highest in summer, with a maximum value at about 1.25 km at 13:00. By contrast, the height of the high-value zone of the aerosol extinction coefficient was lowest in winter, with a maximum of about 0.7 km at 14:00. The maximum height in both spring and autumn was about 0.8 km at 12:00.

We have discussed the influence and interconnections of the vertical distribution of aerosols, the meteorological conditions within the boundary layer and the optical properties of aerosols during a haze event in Beijing. During PE2, the updraft promoted the accumulation of pollutants between 0.5 and 1.5 km. Together with the hygroscopic growth of aerosol particles, this led to a gradual increase in AOD_{440nm}, but the $PM_{2.5}$ mass concentration did not change significantly. A sinking airflow of 1–1.5 m s^{-1} appeared around 11:00, which transported pollutants from high altitudes to the near-surface, promoting a rapid increase in the $PM_{2.5}$ mass concentration. Scattered spherical fine particles dominated this heavy haze pollution event.

Supplementary Materials: The following supporting information can be downloaded at: https://www.mdpi.com/article/10.3390/rs15020475/s1, Figure S1. Vertical profile of the aerosol extinction coefficients in urban Beijing from 18:00 on 10 February to 17:00 on 11 February 2020.

Author Contributions: Conceptualization, H.C. and X.Z. (Xiaoye Zhang); methodology, X.Z. (Xinglu Zhang) and Y.Z.; validation, K.G. and X.Z. (Xindan Zhang); formal analysis, H.Z. (Hujia Zhao) and Y.L. (Yuanxin Liang); resources, L.L. and W.Y.; data curation, H.Z. (Hengheng Zhao) and Y.L. (Yanting Lu); writing—original draft preparation, X.Z. (Xinglu Zhang) and Y.Z. writing—review and editing, H.C.; All authors have read and agreed to the published version of the manuscript.

Funding: This research was funded by the Key Research Project, Young Scholars Fund and National Distinguished Young Scholars Fund of National Natural Science Foundation of China (Grant Nos. 42030608, 42105138 and 41825011), General Project of National Natural Science Foundation (Grant Nos. 41975161, 41905117, 42175153), the Basic Research Fund of CAMS (Grant Nos. 2021Y003) and Gansu Province Science and Technology Fund Project of Young Scholars (Grant Nos. 21JR7RA705).

Data Availability Statement: Datasets used in the present study are available from the corresponding author on reasonable request.

Acknowledgments: We are grateful to the CMA of China for providing sounding meteorological data products and near-surface meteorological data products.

Conflicts of Interest: The authors declare no conflict of interest.

References

1. Zhang, X. Study of atmospheric aerosols and their climate effects in China. *Adv. Earth Sci.* **2007**, *1*, 12–16.
2. Zhang, J.; Gong, C.; Huang, C.; Li, J. Raman LiDAR detection of aerosol optical properties. *J. Photonics* **2010**, *39*, 1340–1344.
3. Samoli, E.; Peng, R.; Ramsay, T.; Pipikou, M.; Touloumi, G.; Dominici, F.; Burnett, R.; Cohen, A.; Krewski, D.; Samet, J.; et al. Acute Effects of Ambient Particulate Matter on Mortality in Europe and North America: Results from the APHENA Study. *Environ. Health Perspect.* **2008**, *116*, 1480–1486. [CrossRef] [PubMed]
4. Zhang, X.; Sun, J.; Wang, Y.; Li, W.; Zhang, Q.; Wang, W.; Quan, J.; Cao, G.; Wang, J.; Yang, Y.; et al. Thinking about the causes of fog and haze in China and its management. *Chin. Sci. Bull.* **2013**, *58*, 1178–1187.
5. Smith, J.D.; Mitsakou, C.; Kitwiroon, N.; Barratt, B.M.; Walton, H.A.; Taylor, J.G.; Anderson, H.R.; Kelly, F.J.; Beevers, S.D. London Hybrid Exposure Model: Improving Human Exposure Estimates to NO2 and PM2.5 in an Urban Setting. *Environ. Sci. Technol.* **2016**, *50*, 11760–11768. [CrossRef] [PubMed]
6. Pang, Y.; Huang, W.; Luo, X.-S.; Chen, Q.; Zhao, Z.; Tang, M.; Hong, Y.; Chen, J.; Li, H. In-Vitro Human Lung Cell Injuries Induced by Urban PM2.5 during a Severe Air Pollution Episode: Variations Associated with Particle Components. *Ecotoxicol. Environ. Saf.* **2020**, *206*, 111406. [CrossRef]
7. Zhao, H.; Gui, K.; Ma, Y.; Wang, Y.; Wang, Y.; Wang, H.; Dou, Y.; Zheng, Y.; Li, L.; Zhang, L.; et al. Effects of Different Aerosols on the Air Pollution and Their Relationship With Meteorological Parameters in North China Plain. *Front. Environ. Sci.* **2022**, *54*, 814736. [CrossRef]
8. Xing, C.; Liu, C.; Wang, S.; Chan, K.L.; Gao, Y.; Huang, X.; Su, W.; Zhang, C.; Dong, Y.; Fan, G.; et al. Observations of the Vertical Distributions of Summertime Atmospheric Pollutants and the Corresponding Ozone Production in Shanghai, China. *Atmos. Chem. Phys.* **2017**, *17*, 14275–14289. [CrossRef]
9. Xing, C.; Liu, C.; Hu, Q.; Fu, Q.; Wang, S.; Lin, H.; Zhu, Y.; Wang, S.; Wang, W.; Javed, Z.; et al. Vertical Distributions of Wintertime Atmospheric Nitrogenous Compounds and the Corresponding OH Radicals Production in Leshan, Southwest China. *J. Environ. Sci.* **2021**, *105*, 44–55. [CrossRef]
10. Twomey, S. The Influence of Pollution on the Shortwave Albedo of Clouds. *J. Atmos. Sci.* **1977**, *34*, 1149–1152. [CrossRef]
11. Dubovik, O.; King, M.D. A Flexible Inversion Algorithm for Retrieval of Aerosol Optical Properties from Sun and Sky Radiance Measurements. *J. Geophys. Res.-Atmos.* **2000**, *105*, 20673–20696. [CrossRef]
12. Eck, T.F.; Holben, B.N.; Reid, J.S.; Giles, D.M.; Rivas, M.A.; Singh, R.P.; Tripathi, S.N.; Bruegge, C.J.; Platnick, S.; Arnold, G.T.; et al. Fog- and Cloud-Induced Aerosol Modification Observed by the Aerosol Robotic Network (AERONET). *J. Geophys. Res.-Atmos.* **2012**, *117*, D07206. [CrossRef]
13. Che, H.; Xia, X.; Zhu, J.; Wang, H.; Wang, Y.; Sun, J.; Zhang, X.; Shi, G. Aerosol Optical Properties under the Condition of Heavy Haze over an Urban Site of Beijing, China. *Environ. Sci. Pollut. Res.* **2015**, *22*, 1043–1053. [CrossRef] [PubMed]
14. Che, H.; Zhang, X.-Y.; Xia, X.; Goloub, P.; Holben, B.; Zhao, H.; Wang, Y.; Zhang, X.-C.; Wang, H.; Blarel, L.; et al. Ground-Based Aerosol Climatology of China: Aerosol Optical Depths from the China Aerosol Remote Sensing Network (CARSNET) 2002–2013. *Atmos. Chem. Phys.* **2015**, *15*, 7619–7652. [CrossRef]
15. Che, H.; Zhao, H.; Wu, Y.; Xia, X.; Zhu, J.; Wang, H.; Wang, Y.; Sun, J.; Yu, J.; Zhang, X.; et al. Analyses of Aerosol Optical Properties and Direct Radiative Forcing over Urban and Industrial Regions in Northeast China. *Meteorol. Atmos. Phys.* **2015**, *127*, 345–354. [CrossRef]
16. Zheng, Y.; Che, H.; Zhao, T.; Zhao, H.; Gui, K.; Sun, T.; An, L.; Yu, J.; Liu, C.; Jiang, Y.; et al. Aerosol Optical Properties Observation and Its Relationship to Meteorological Conditions and Emission during the Chinese National Day and Spring Festival Holiday in Beijing. *Atmos. Res.* **2017**, *197*, 188–200. [CrossRef]
17. Ackerman, A.S.; Kirkpatrick, M.P.; Stevens, D.E.; Toon, O.B. The Impact of Humidity above Stratiform Clouds on Indirect Aerosol Climate Forcing. *Nature* **2004**, *432*, 1014–1017. [CrossRef] [PubMed]
18. Wu, D.; Liu, B.; Qi, F.; Fan, A.; Wang, B.; Zhong, Z.; Bo, G.; Liu, D.; Zhou, J.; Wang, Y. Raman-Mie LiDAR measurements of tropospheric atmospheric aerosol optical properties. *J. Atmos. Environ. Opt.* **2011**, *6*, 18–26.
19. Yang, X.; Zhao, C.; Guo, J.; Wang, Y. Intensification of Aerosol Pollution Associated with Its Feedback with Surface Solar Radiation and Winds in Beijing. *J. Geophys. Res.-Atmos.* **2016**, *121*, 4093–4099. [CrossRef]
20. IPCC. *IPCC Sixth Assessment Report: Climate Change 2022*; IPCC: Geneva, Switzerland, 2022.
21. Zheng, Y.; Che, H.; Xia, X.; Wang, Y.; Wang, H.; Wu, Y.; Tao, J.; Zhao, H.; An, L.; Li, L.; et al. Five-Year Observation of Aerosol Optical Properties and Its Radiative Effects to Planetary Boundary Layer during Air Pollution Episodes in North China: Intercomparison of a Plain Site and a Mountainous Site in Beijing. *Sci. Total Environ.* **2019**, *674*, 140–158. [CrossRef]
22. Che, H.; Zhang, X.; Chen, H.; Damiri, B.; Goloub, P.; Li, Z.; Zhang, X.; Wei, Y.; Zhou, H.; Dong, F.; et al. Instrument Calibration and Aerosol Optical Depth Validation of the China Aerosol Remote Sensing Network. *J. Geophys. Res.-Atmos.* **2009**, *114*, D03206. [CrossRef]
23. Sheng, Z.; Che, H.; Chen, Q.; Xia, X.; Liu, D.; Wang, Z.; Zhao, H.; Gui, K.; Zheng, Y.; Sun, T.; et al. Aerosol Vertical Distribution and Optical Properties of Different Pollution Events in Beijing in Autumn 2017. *Atmos. Res.* **2019**, *215*, 193–207. [CrossRef]

24. Luo, X.-S.; Zhao, Z.; Chen, Y.; Ge, X.; Huang, Y.; Suo, C.; Sun, X.; Zhang, D. Effects of Emission Control and Meteorological Parameters on Urban Air Quality Showed by the 2014 Youth Olympic Games in China. *Fresenius Environ. Bull.* **2017**, *26*, 4798–4807.
25. Li, J.; Gao, W.; Cao, L.; Xiao, Y.; Zhang, Y.; Zhao, S.; Liu, Z.; Liu, Z.; Tang, G.; Ji, D.; et al. Significant Changes in Autumn and Winter Aerosol Composition and Sources in Beijing from 2012 to 2018: Effects of Clean Air Actions. *Environ. Pollut.* **2021**, *268*, 115855. [CrossRef]
26. Liang, Y.; Che, H.; Wang, H.; Peng, Y.; Zhang, Y.; Tao, F. Aerosol optical properties and radiation effects of primary pollution processes in Beijing. *J. Appl. Meteorol. Sci.* **2020**, *31*, 583–594.
27. Liang, Y.; Che, H.; Wang, H.; Zhang, W.; Li, L.; Zheng, Y.; Gui, K.; Zhang, P.; Zhang, X. Aerosols Direct Radiative Effects Combined Ground-Based Lidar and Sun-Photometer Observations: Cases Comparison between Haze and Dust Events in Beijing. *Remote Sens.* **2022**, *14*, 266. [CrossRef]
28. Pace, G.; Junkermann, W.; Vitali, L.; Di Sarra, A.; Meloni, D.; Cacciani, M.; Cremona, G.; Iannarelli, A.M.; Zanini, G. On the Complexity of the Boundary Layer Structure and Aerosol Vertical Distribution in the Coastal Mediterranean Regions: A Case Study. *Tellus Ser. B-Chem. Phys. Meteorol.* **2015**, *67*, 27721. [CrossRef]
29. Huige, D.; Siwen, L.; Yun, Y.; Dengxin, H.; Jianyu, W. Observational Study of the Vertical Aerosol and Meteorological Factor Distributions with Respect to Particulate Pollution in Xi'an. *Atmos. Environ.* **2021**, *247*, 118215. [CrossRef]
30. Zhu, J.; Zhu, B.; Huang, Y.; An, J.; Xu, J. PM2.5 Vertical Variation during a Fog Episode in a Rural Area of the Yangtze River Delta, China. *Sci. Total Environ.* **2019**, *685*, 555–563. [CrossRef]
31. Liu, C.; Huang, J.; Wang, Y.; Tao, X.; Hu, C.; Deng, L.; Xu, J.; Xiao, H.-W.; Luo, L.; Xiao, H.-Y.; et al. Vertical Distribution of PM2.5 and Interactions with the Atmospheric Boundary Layer during the Development Stage of a Heavy Haze Pollution Event. *Sci. Total Environ.* **2020**, *704*, 135329. [CrossRef]
32. Xia, X.; Li, Z.; Holben, B.; Wang, P.; Eck, T.; Chen, H.; Cribb, M.; Zhao, Y. Aerosol Optical Properties and Radiative Effects in the Yangtze Delta Region of China. *J. Geophys. Res.-Atmos.* **2007**, *112*, D22S12. [CrossRef]
33. Xia, X.; Chen, H.; Goloub, P.; Zong, X.; Zhang, W.; Wang, P. Climatological Aspects of Aerosol Optical Properties in North China Plain Based on Ground and Satellite Remote-Sensing Data. *J. Quant. Spectrosc. Radiat. Transf.* **2013**, *127*, 12–23. [CrossRef]
34. Wang, H.; Shi, G.Y.; Zhang, X.Y.; Gong, S.L.; Tan, S.C.; Chen, B.; Che, H.Z.; Li, T. Mesoscale Modelling Study of the Interactions between Aerosols and PBL Meteorology during a Haze Episode in China Jing–Jin–Ji and Its near Surrounding Region–Part 2: Aerosols' Radiative Feedback Effects. *Atmos. Chem. Phys.* **2015**, *15*, 3277–3287. [CrossRef]
35. Zhao, H.; Wu, Z.; Liu, J.; Wu, G. Two Air Pollution Events in the Coastal City of Tianjin, North China Plain. *Atmos. Pollut. Res.* **2019**, *10*, 1780–1794. [CrossRef]
36. Yang, X.; Lu, Y.; Zhu, X.; He, J.; Jiang, Q.; Wu, K.; Wang, H.; Zhang, X.; Wang, S. Formation and Evolution Mechanisms of Severe Haze Pollution in the Sichuan Basin, Southwest China. *Aerosol. Air Qual. Res.* **2020**, *20*, 2557–2567. [CrossRef]
37. Liu, Y.; Zhao, H.; Ma, Y.; Yang, H.; Wang, Y.; Wang, H.; Zhang, Y.; Zou, X.; Wang, H.; Wen, R.; et al. Characteristics of Particulate Matter and Meteorological Conditions of a Typical Air-Pollution Episode in Shenyang, Northeastern China, in Winter 2017. *Atmos. Pollut. Res.* **2021**, *12*, 316–327. [CrossRef]
38. Xing, C.; Liu, C.; Hong, Q.; Liu, H.; Wu, H.; Lin, J.; Song, Y.; Chen, Y.; Liu, T.; Hu, Q.; et al. Vertical Distributions and Potential Sources of Wintertime Atmospheric Pollutants and the Corresponding Ozone Production on the Coast of Bohai Sea. *J. Environ. Manag.* **2022**, *319*, 115721. [CrossRef]
39. Zhang, H.; Wang, Y.; Hu, J.; Ying, Q.; Hu, X.-M. Relationships between Meteorological Parameters and Criteria Air Pollutants in Three Megacities in China. *Environ. Res.* **2015**, *140*, 242–254. [CrossRef]
40. Wang, P.; Cao, J.; Tie, X.; Wang, G.; Li, G.; Hu, T.; Wu, Y.; Xu, Y.; Xu, G.; Zhao, Y.; et al. Impact of Meteorological Parameters and Gaseous Pollutants on PM2.5 and PM10 Mass Concentrations during 2010 in Xi'an, China. *Aerosol. Air Qual. Res.* **2015**, *15*, 1844–1854. [CrossRef]
41. Shi, Z.; Huang, L.; Li, J.; Ying, Q.; Zhang, H.; Hu, J. Sensitivity Analysis of the Surface Ozone and Fine Particulate Matter to Meteorological Parameters in China. *Atmos. Chem. Phys.* **2020**, *20*, 13455–13466. [CrossRef]
42. Chen, Y.; Xie, S. Long-Term Trends and Characteristics of Visibility in Two Megacities in Southwest China: Chengdu and Chongqing. *J. Air Waste Manag. Assoc.* **2013**, *63*, 1058–1069. [CrossRef]
43. Chen, W.; Zhang, S.; Tong, Q.; Zhang, X.; Zhao, H.; Ma, S.; Xiu, A.; He, Y. Regional Characteristics and Causes of Haze Events in Northeast China. *Chin. Geogr. Sci.* **2018**, *28*, 836–850. [CrossRef]
44. Qiao, Z.; Wu, F.; Xu, X.; Yang, J.; Liu, L. Mechanism of Spatiotemporal Air Quality Response to Meteorological Parameters: A National-Scale Analysis in China. *Sustainability* **2019**, *11*, 3957. [CrossRef]
45. Ji, M.; Jiang, Y.; Han, X.; Liu, L.; Xu, X.; Qiao, Z.; Sun, W. Spatiotemporal Relationships between Air Quality and Multiple Meteorological Parameters in 221 Chinese Cities. *Complexity* **2020**, *2020*, e6829142. [CrossRef]
46. Zhang, X.; Zhong, J.; Wang, J.; Wang, Y.; Liu, Y. The Interdecadal Worsening of Weather Conditions Affecting Aerosol Pollution in the Beijing Area in Relation to Climate Warming. *Atmos. Chem. Phys.* **2018**, *18*, 5991–5999. [CrossRef]
47. Jin, L.; Luo, X.; Fu, P.; Li, X. Airborne Particulate Matter Pollution in Urban China: A Chemical Mixture Perspective from Sources to Impacts. *Natl. Sci. Rev.* **2017**, *4*, 593–610. [CrossRef]
48. Zhong, J.; Zhang, X.; Wang, Y. Relatively Weak Meteorological Feedback Effect on PM2.5 Mass Change in Winter 2017/18 in the Beijing Area: Observational Evidence and Machine-Learning Estimations. *Sci. Total Environ.* **2019**, *664*, 140–147. [CrossRef]

49. Yang, S.; Duan, F.; Ma, Y.; Li, H.; Ma, T.; Zhu, L.; Huang, T.; Kimoto, T.; He, K. Mixed and Intensive Haze Pollution during the Transition Period between Autumn and Winter in Beijing, China. *Sci. Total Environ.* **2020**, *711*, 134745. [CrossRef] [PubMed]
50. Zhong, J.; Zhang, X.; Dong, Y.; Wang, Y.; Liu, C.; Wang, J.; Zhang, Y.; Che, H. Feedback Effects of Boundary-Layer Meteorological Factors on Cumulative Explosive Growth of PM2.5 during Winter Heavy Pollution Episodes in Beijing from 2013 to 2016. *Atmos. Chem. Phys.* **2018**, *18*, 247–258. [CrossRef]
51. Zhong, J.; Zhang, X.; Wang, Y.; Liu, C.; Dong, Y. Heavy Aerosol Pollution Episodes in Winter Beijing Enhanced by Radiative Cooling Effects of Aerosols. *Atmos. Res.* **2018**, *209*, 59–64. [CrossRef]
52. Zhong, J.; Zhang, X.; Wang, Y.; Sun, J.; Shen, X.; Xia, C.; Zhang, W. Attribution of the Worse Aerosol Pollution in March 2018 in Beijing to Meteorological Variability. *Atmos. Res.* **2021**, *250*, 105294. [CrossRef]
53. Xu, Q.; Wang, S.; Jiang, J.; Bhattarai, N.; Li, X.; Chang, X.; Qiu, X.; Zheng, M.; Hua, Y.; Hao, J. Nitrate Dominates the Chemical Composition of PM2.5 during Haze Event in Beijing, China. *Sci. Total Environ.* **2019**, *689*, 1293–1303. [CrossRef] [PubMed]
54. Zhang, T.; Che, H.; Gong, Z.; Wang, Y.; Wang, J.; Yang, Y.; Gui, K.; Guo, B. The Two-Way Feedback Effect between Aerosol Pollution and Planetary Boundary Layer Structure on the Explosive Rise of PM2.5 after the "Ten Statements of Atmosphere" in Beijing. *Sci. Total Environ.* **2020**, *709*, 136259. [CrossRef]
55. Zhang, T.; Che, H.; Gong, Z.; Wang, Y.; Wang, J.; Yang, Y. The Dominant Mechanism of the Explosive Rise of PM2.5 after Significant Pollution Emissions Reduction in Beijing from 2017 to the COVID-19 Pandemic in 2020. *Atmos. Pollut. Res.* **2021**, *12*, 272–281. [CrossRef]
56. Sheng, Z. Detection of Aerosol Optical-Radiometric Properties in Urban Beijing Based on Multi-Band Photometry and LiDAR. Master's Thesis, Chengdu University of Information Technology, Chengdu, China, 2019.
57. Che, H.; Yang, Z.; Zhang, X.; Zhu, C.; Ma, Q.; Zhou, H.; Wang, P. Study on the Aerosol Optical Properties and Their Relationship with Aerosol Chemical Compositions over Three Regional Background Stations in China. *Atmos. Environ.* **2009**, *43*, 1093–1099. [CrossRef]
58. Zhao, H. Study on the Optical Properties of Atmospheric Aerosols and Their Direct Radiation Effects in Urban Areas of Northeastern China. Ph.D. Dissertation, Chinese Academy of Meteorological Sciences, Beijing, China, 2014.
59. Zheng, Y.; Che, H.; Yang, L.; Chen, J.; Wang, Y.; Xia, X.; Zhao, H.; Wang, H.; Wang, D.; Gui, K.; et al. Optical and Radiative Properties of Aerosols during a Severe Haze Episode over the North China Plain in December 2016. *J. Meteorol. Res.* **2017**, *31*, 1045–1061. [CrossRef]
60. Dubovik, O.; Sinyuk, A.; Lapyonok, T.; Holben, B.N.; Mishchenko, M.; Yang, P.; Eck, T.F.; Volten, H.; Muñoz, O.; Veihelmann, B.; et al. Application of Spheroid Models to Account for Aerosol Particle Nonsphericity in Remote Sensing of Desert Dust. *J. Geophys. Res. Atmos.* **2006**, *111*. [CrossRef]
61. Che, H.; Xia, X.; Zhu, J.; Li, Z.; Dubovik, O.; Holben, B.; Goloub, P.; Chen, H.; Estelles, V.; Cuevas-Agulló, E.; et al. Column Aerosol Optical Properties and Aerosol Radiative Forcing during a Serious Haze-Fog Month over North China Plain in 2013 Based on Ground-Based Sunphotometer Measurements. *Atmos. Chem. Phys.* **2014**, *14*, 2125–2138. [CrossRef]
62. Wang, J.; Yang, Y.; Zhang, X.; Liu, H.; Che, H.; Shen, X.; Wang, Y. On the Influence of Atmospheric Super-Saturation Layer on China's Heavy Haze-Fog Events. *Atmos. Environ.* **2017**, *171*, 261–271. [CrossRef]
63. Tao, N.; Wang, J.; Yang, Y.; Jiang, X.; Jiang, Y.; Che, H. The Impact of the Large-Scale Circulation Anomalies in the Northern Hemisphere on Air Quality in Wuhan of China during the Spring Festival in 2020. *J. Atmos. Sol.-Terr. Phys.* **2022**, *238*, 105931. [CrossRef]
64. Wallace, J.M.; Hobbs, P.V. *Atmosphere Science*; Elsevier: Amsterdam, The Netherlands, 2008; Volume 486.
65. Zhang, Y.; Guo, J.; Yang, Y.; Wang, Y.; Yim, S.H.L. Vertical Wind Shear Modulates Particulate Matter Pollutions: A Perspective from Radar Wind Profiler Observations in Beijing, China. *Remote Sens.* **2020**, *12*, 546. [CrossRef]
66. Kang, B.; Liu, C.; Miao, C.; Zhang, T.; Li, Z.; Hou, C.; Li, H.; Li, C.; Zheng, Y.; Che, H. A Comprehensive Study of a Winter Haze Episode over the Area around Bohai Bay in Northeast China: Insights from Meteorological Elements Observations of Boundary Layer. *Sustainability* **2022**, *14*, 5424. [CrossRef]
67. Sun, T. Study on Vertical Observation of Aerosol Optical-Radiative Properties in Hangzhou Area. Master's Thesis, Chinese Academy of Meteorological Sciences, Beijing, China, 2018.
68. Sun, J.; Zhang, L.; Shen, X.; Che, H.; Zhang, Y.; Fan, R.; Ma, Q.; Yue, Y.; Yu, X. Progress in the study of scattering hygroscopic growth characteristics of atmospheric aerosols. *ACTA Meteorol. Sin.* **2016**, *74*, 672–682.
69. Qi, X. Observational Study on the Growth Characteristics of Atmospheric Aerosol Scattering Hygroscopicity in North China. Master's Thesis, Chinese Academy of Meteorological Sciences, Beijing, China, 2018.
70. Xiang, Y.; Zhang, T.; Liu, J.; Lv, L.; Dong, Y.; Chen, Z. Atmosphere Boundary Layer Height and Its Effect on Air Pollutants in Beijing during Winter Heavy Pollution. *Atmos. Res.* **2019**, *215*, 305–316. [CrossRef]
71. Liu, B.; Ma, Y.; Guo, J.; Gong, W.; Zhang, Y.; Mao, F.; Li, J.; Guo, X.; Shi, Y. Boundary Layer Heights as Derived From Ground-Based Radar Wind Profiler in Beijing. *IEEE Trans. Geosci. Remote Sens.* **2019**, *57*, 8095–8104. [CrossRef]
72. Solanki, R.; Guo, J.; Li, J.; Singh, N.; Guo, X.; Han, Y.; Lv, Y.; Zhang, J.; Liu, B. Atmospheric-Boundary-Layer-Height Variation over Mountainous and Urban Sites in Beijing as Derived from Radar Wind-Profiler Measurements. *Bound.-Layer Meteor.* **2021**, *181*, 125–144. [CrossRef]
73. Miao, Y.; Che, H.; Zhang, X.; Liu, S. Integrated Impacts of Synoptic Forcing and Aerosol Radiative Effect on Boundary Layer and Pollution in the Beijing-Tianjin-Hebei Region, China. *Atmos. Chem. Phys.* **2020**, *20*, 5899–5909. [CrossRef]

74. Fan, F.; Chen, Y.; Lu, J.; Zhao, Y.; Gao, J.; Chai, F.; Dong, S. LiDAR observations before and after the strong dust process in Beijing in spring. *Res. Environ. Sci.* **2013**, *26*, 1155–1161. [CrossRef]
75. Yao, W.; Che, H.; Gui, K.; Wang, Y.; Zhang, X. Can MERRA-2 Reanalysis Data Reproduce the Three-Dimensional Evolution Characteristics of a Typical Dust Process in East Asia? A Case Study of the Dust Event in May 2017. *Remote Sens.* **2020**, *12*, 902. [CrossRef]
76. Ren, H.; Li, A.; Xie, P.; Hu, Z.; Xu, J.; Huang, Y.; Li, X.; Zhong, H.; Zhang, H.; Tian, X.; et al. The Characterization of Haze and Dust Processes Using MAX-DOAS in Beijing, China. *Remote Sens.* **2021**, *13*, 5133. [CrossRef]
77. Ma, Y.; Ye, J.; Xin, J.; Zhang, W.; de Arellano, J.V.-G.; Wang, S.; Zhao, D.; Dai, L.; Ma, Y.; Wu, X.; et al. The Stove, Dome, and Umbrella Effects of Atmospheric Aerosol on the Development of the Planetary Boundary Layer in Hazy Regions. *Geophys. Res. Lett.* **2020**, *47*, e2020GL087373. [CrossRef]
78. Ma, Y. How Do Aerosols above the Residual Layer Affect the Planetary Boundary Layer Height? *Sci. Total Environ.* **2022**, *9*, 151953. [CrossRef] [PubMed]
79. Li, L.; Zhou, M.; Li, X. The interaction between nocturnal urban atmospheric boundary layer and aerosols. *J. Appl. Meteorol. Sci.* **1992**, *3*, 32–41.
80. Moradi, I.; Arkin, P.; Ferraro, R.; Eriksson, P.; Fetzer, E. Diurnal Variation of Tropospheric Relative Humidity in Tropical Regions. *Atmos. Chem. Phys.* **2016**, *16*, 6913–6929. [CrossRef]
81. He, J. Air Pollution Characteristics and Their Relation to Meteorological Conditions during 2014–2015 in Major Chinese Cities. *Environ. Pollut.* **2017**, *223*, 484–496. [CrossRef]
82. Giles, D.M.; Holben, B.N.; Eck, T.F.; Sinyuk, A.; Smirnov, A.; Slutsker, I.; Dickerson, R.R.; Thompson, A.M.; Schafer, J.S. An Analysis of AERONET Aerosol Absorption Properties and Classifications Representative of Aerosol Source Regions. *J. Geophys. Res.-Atmos.* **2012**, *117*, D17203. [CrossRef]
83. Zhang, Y.; Li, Z.; Cuesta, J.; Li, D.; Wei, P.; Xie, Y.; Li, L. Aerosol Column Size Distribution and Water Uptake Observed during a Major Haze Outbreak over Beijing on January 2013. *Aerosol. Air Qual. Res.* **2015**, *15*, 945–957. [CrossRef]
84. Russell, P.B.; Bergstrom, R.W.; Shinozuka, Y.; Clarke, A.D.; DeCarlo, P.F.; Jimenez, J.L.; Livingston, J.M.; Redemann, J.; Dubovik, O.; Strawa, A. Absorption Angstrom Exponent in AERONET and Related Data as an Indicator of Aerosol Composition. *Atmos. Chem. Phys.* **2010**, *10*, 1155–1169. [CrossRef]
85. Zhang, Y.-L.; Cao, F. Fine Particulate Matter (PM2.5) in China at a City Level. *Sci. Rep.* **2015**, *5*, 14884. [CrossRef]
86. Zhang, R.; Wang, G.; Guo, S.; Zarnora, M.L.; Ying, Q.; Lin, Y.; Wang, W.; Hu, M.; Wang, Y. Formation of Urban Fine Particulate Matter. *Chem. Rev.* **2015**, *115*, 3803–3855. [CrossRef]
87. Wu, L.; Zhang, X.; Sun, J.; Wang, Y.; Zhong, J.; Meng, Z. Intensified Wintertime Secondary Inorganic Aerosol Formation during Heavy Haze Pollution Episodes (HPEs) in Beijing, China. *J. Environ. Sci.* **2022**, *114*, 503–513. [CrossRef] [PubMed]
88. Chi, Q. Study on the Spatial and Temporal Distribution and Transformation Mechanism of Ozone and Secondary Inorganic Aerosol Formation in North China. Ph.D. Dissertation, University of Science and Technology of China, Beijing, China, 2018.
89. Wang, Q.; Yu, Y.; Meng, M.; Jiang, Q.; Zhang, T.; Chao, N.; Wu, D.; Wu, J. Analysis of the causes of atmospheric PM_(2.5) pollution in a typical city in Zhejiang during a period of heavy air pollution in the Yangtze River Delta. *Environ. Pollut. Prev.* **2019**, *41*, 1076–1081. [CrossRef]
90. Han, L.; Yan, H.; Xiang, X.; Liu, X.; Shi, R.; Wang, H.; Cheng, S.; Wang, H. Characteristics, Evolution, and Potential Source Regions of Submicron Aerosol in Beijing, China. *Atmos. Environ.* **2021**, *246*, 118061. [CrossRef]

Disclaimer/Publisher's Note: The statements, opinions and data contained in all publications are solely those of the individual author(s) and contributor(s) and not of MDPI and/or the editor(s). MDPI and/or the editor(s) disclaim responsibility for any injury to people or property resulting from any ideas, methods, instructions or products referred to in the content.